Acta Materialia 285 (2025) 120648

Contents lists available at ScienceDirect

Acta Materialia

journal homepage: www.elsevier.com/locate/actamat

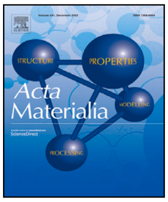

Full length article

Effects of Y solutes on the activation of the $\{11\bar{2}1\}\langle\bar{1}\bar{1}26\rangle$ deformation twinning in MgY solid solution alloys

Jianwei Xiao [a,b], Junjie Gao [a], Songwei Li [a], Rui Wang [a], Chuang Deng [c], Yuntian Zhu [a,d], Zhaoxuan Wu [a,d,*]

[a] Department of Materials Science and Engineering, City University of Hong Kong, Hong Kong Special Administrative Region of China
[b] Shenyang National Laboratory for Materials Science, Institute of Metal Research, Chinese Academy of Sciences, 72 Wenhua Road, Shenyang 110016, China
[c] Department of Mechanical Engineering, University of Manitoba, Winnipeg, MB R3T 5V6, Canada
[d] Hong Kong Institute for Advanced Study, City University of Hong Kong, Hong Kong Special Administrative Region of China

ARTICLE INFO

Keywords:
Mg rare earth alloys
Deformation twinning
Nucleation mechanism
Density-functional theory calculations

ABSTRACT

The $\{11\bar{2}1\}\langle\bar{1}\bar{1}26\rangle$ deformation twin is common in nominally pure HCP Ti, Zr, Re, Co, but not in Mg. Rare-earth (RE) solutes such as Y and Gd at low atomic concentrations, however, can activate this twin mode and make it competitive to the regular $\{10\bar{1}2\}\langle\bar{1}011\rangle$ extension twin in Mg. Previously models have not explicitly revealed the role of RE solutes on twinning and the RE-effects remain poorly understood. Using a reduced-constraint (RC) slip path, DFT calculations and two newly-developed interatomic potentials for MgY and MgAl, we reveal the physical origin of the RE solute effects in activating the $\{11\bar{2}1\}\langle\bar{1}\bar{1}26\rangle$ twin in MgY alloys with random and short range order solute states. The RC-path shows that localized slip in the $\langle\bar{1}\bar{1}26\rangle$ twinning direction simultaneously drives shear and $\langle 1\bar{1}00\rangle$-direction shuffle displacements on the corrugated $\{11\bar{2}1\}$ twinning plane. The shuffle displacements are essential to reverse the asymmetry of $\{1\bar{1}00\}$ atom-planes to satisfy the twin symmetry. However, such shuffle displacements are insufficient in pure Mg or MgAl, leaving twin nucleation to the multi-layer slip path with high energy barriers. Y-solutes are able to enhance the slip-driven shuffling to levels sufficient to reverse the $\{1\bar{1}00\}$ atom-planes asymmetry, leading to spontaneous nucleation of multi-layer twin embryo with reduced energy barriers lower than that for the competing $\{10\bar{1}2\}\langle\bar{1}011\rangle$ extension twin in Mg. The RC-slip path and $\{11\bar{2}1\}\langle\bar{1}\bar{1}26\rangle$ twin nucleation is directly demonstrated in atomistic simulations of a blunted cracks under mode-II loading. This slip driven, solute-modulated twin nucleation mechanism is expected to be general across all HCP metals and alloys.

1. Introduction

HCP metals have complex and disparate dislocation slip systems [1,2]. The $\langle \mathbf{a} \rangle$ slip typically has low critical resolved shear stresses (CRSS), but cannot provide plastic strain accommodation in the crystallographic $\langle \mathbf{c} \rangle$ direction. Slip in the $\langle \mathbf{c} \rangle$ direction cannot be carried out by $\langle \mathbf{c} \rangle$ dislocations as their edge or mixed segments have climb-dissociated sessile cores [3,4]. Normal strain in the $\langle \mathbf{c} \rangle$ direction cannot be provided by glide of $\langle \mathbf{c} \rangle$ dislocations even if they were highly mobile. The $\langle \mathbf{c}+\mathbf{a} \rangle$ slip is thus necessary, but nucleation of $\langle \mathbf{c}+\mathbf{a} \rangle$ dislocations passes through high energy barriers, requiring considerably higher stresses to activate [5,6]. Glide of $\langle \mathbf{c}+\mathbf{a} \rangle$ dislocations can also be limited by transformation to climb-dissociated sessile cores [4,7]. Alternatively, deformation twinning is activated as a secondary deformation mechanism in the family of HCP metals [8]. The activation of twinning is complex and depends on multiple factors, including loading conditions, temperature, grain sizes [9] and alloying compositions [10]. The activated twinning modes also differ within the HCP family [1]. Ti and Zr have at least 4 active twinning modes, while others have less. Mg has 2 common twinning modes: the $\{10\bar{1}2\}\langle\bar{1}011\rangle$ extension and $\{10\bar{1}1\}\langle 10\bar{1}\bar{2}\rangle$ contraction twins. The $\{11\bar{2}1\}\langle\bar{1}\bar{1}26\rangle$ extension twin (Fig. 1a,b), common in Ti [11], Zr [12], Re [13] and Co [14], has never been *experimentally* observed in *pure* Mg. However, this twin mode is activated and can be prevalent in Mg alloyed with rare-earth (RE) solutes (MgY [15–17], WE54 [18], MgGd [19,20], Mg–RE [21,22]). Despite a number of early studies [16,17,20,23], the physical origin of the RE effects on the $\{11\bar{2}1\}\langle\bar{1}\bar{1}26\rangle$ twin activation is not well understood in Mg.

The criteria for the onset of deformation twinning are well-established in elemental FCC metals and alloys. Twinning in FCC can

---

* Corresponding author at: Department of Materials Science and Engineering, City University of Hong Kong, Hong Kong Special Administrative Region of China.

E-mail address: zhaoxuwu@cityu.edu.hk (Z. Wu).

https://doi.org/10.1016/j.actamat.2024.120648
Received 22 May 2024; Received in revised form 3 December 2024; Accepted 9 December 2024

occur by sequential atomic slips in the $\langle 11\bar{2}\rangle$ direction on consecutive close-packed $\{111\}$ planes. The energetics of these slip processes can be robustly described by the generalized stacking fault energy (GSFE [24]) and generalized planar fault energy (GPFE [25]) profiles with characteristic unstable, metastable (local minima) and twin fault energies, i.e., γ_{us}, γ_{isf} and γ_{utf}. The critical loading for twin nucleation can be quantitatively predicted using a Peierls criterion at crack-tips [25,26] and grain boundaries (GBs) [27]. With the material-dependent γ_{us}, γ_{isf} and γ_{utf}, the GSFE-based Peierls criterion has successfully established the twinning tendency consistent with experiments across a wide range of FCC structures [25,26,28].

The success of the GSFE-based twinning criterion largely relies on the simple kinetic path during twin nucleation in FCC structures. All FCC metals (except Pt) exhibit a *distinct, metastable* SF, which is a necessary condition for the formation of the first extended SF and is generally required for subsequent twinning. In addition, *slip* across the close-packed $\{111\}$ plane is the dominant atomic displacement during twin nucleation. In HCP (or BCC) structures, however, no metastable intrinsic SF exists on the classical GSFE γ-lines on some twinning planes, making the application of GSFE/GPFE to twinning both conceptually and practically difficult in these structures [29,30]. For example, the present $\{11\bar{2}1\}\langle\bar{1}\bar{1}26\rangle\gamma$-line do not have metastable SF in pure Mg. To circumvent these difficulties, constrained multilayer-slip, built upon early unstable single or multilayer SFs, is introduced to estimate the twin nucleation path and minimum twin thickness [31,32]. However, the imposed constrains reduce or eliminate atom shuffles which are often essential during twin nucleation and growth in non-FCC structures [33]. Furthermore, the matrix-twin may have material-dependent, microscopic degrees of freedom in addition to their macroscopic mirror reflection symmetry [30,31,34], which raises additional variations in the multilayer constrained slip process. The above complexities present great challenges for systematic investigation of twin nucleation and growth in general.

Recently, we employed a reduced-constraint (RC, similar to the modified GSFE [6,30,35]) slip path to unveil the twin nucleation and growth mechanism across BCC transition metals [30,36]. The RC method naturally allows both slip and shuffle displacements across multiple atom-layers, and enables a unified, GSFE-based treatment of dislocation and twin nucleations across all FCC, BCC and HCP structures. The GSFE profile by RC (γ_{rc}) accurately captures the energetics during localized slip displacements and reverts to the classical γ-line if shuffle displacements do not occur (see Refs. [6,30,35] and below). The critical condition for twin nucleation in HCP structures can now be established in a similar Peierls framework as of FCC [25,26] and BCC structures [30].

In this work, we apply the RC method to unveil the $\{11\bar{2}1\}\langle\bar{1}\bar{1}26\rangle$ twinning path and the role of RE-solutes in activating this twin in Mg–RE alloys. In particular, we study the classical and RC-based GSFE γ-lines and associated atom trajectories during localized slip in the $\langle\bar{1}\bar{1}26\rangle$ twinning direction on the $\{11\bar{2}1\}$ twinning plane in pure Mg and Mg with Y or Al solutes. GSFE γ-lines calculated with density-functional theory (DFT) show that multilayer twin embryos are spontaneously nucleated along the γ_{rc} slip path in the presence of Y-solute environment while no twin embryo is formed in *pure* Mg or Mg with Al solutes. The twin nucleation is enabled by Y-solute enhanced atom *shuffle* displacements in the $\langle 1\bar{1}00\rangle$ direction when the local shear or localized slip displacement reaches that corresponding to the $\{11\bar{2}1\}\langle\bar{1}\bar{1}26\rangle$ twinning Burgers vector $\mathbf{b}_t$. Furthermore, the DFT-based GSFE results and effects of Y-solutes are directly demonstrated at crack-tips in atomistic simulations of Mg–1.5at.%Y and Mg–3at.%Y alloys. These MgY simulation results are then cross-compared with that in Mg–3at.%Al where the $\{11\bar{2}1\}$ twin is not observed. The explicit simulations show that the presence of Y solutes at low concentrations (e.g., 3at.%) facilitates both the nucleation and growth of the $\{11\bar{2}1\}\langle\bar{1}\bar{1}26\rangle$, but such effects are not seen with Al solutes or in pure Mg under the same loading conditions. These results are consistent with broad experimental results [15–17,20].

In the following, we first briefly introduce the RC method, the details of the supercells and DFT calculations, followed by the semi-infinite crack models and the interatomic potential used for the direct twin nucleation simulations. The DFT-based classical GSFE γ-line, γ_{rc}-lines, atomic slip and shuffle displacements are then presented for pure Mg, Mg with Y or Al solutes at different configurations. To assess the appropriateness of previous and the present simulations, further comparisons are made with DFT on the corresponding data from extant interatomic potentials commonly used in the literature and the new XMEAM potential. The twin nucleation and growth mechanisms are then presented and compared with the RC slip path used in calculating the γ_{rc}-lines. The critical loads for twin activation in the simulations are benchmarked with the prediction based on the Peierls framework proposed for dislocation nucleation but employed here for twin nucleations. Finally, comparisons with previous twin activation models are then discussed, followed by a brief conclusion and suggestions for further works in the general HCP family of metals and alloys.

2. Computational methods and supercells

2.1. Reduced constraint slip path and GSFE

The $\{11\bar{2}1\}\langle\bar{1}\bar{1}26\rangle$ GSFE γ-lines are calculated using both the classical and RC methods. In both methods and with a slab–vacuum supercell, the crystal is divided into two blocks along the slip/twin plane (i.e., the $\mathbf{K}_1$-$\{11\bar{2}1\}$ plane, Fig. 1c). All atoms above the twin plane (layer 9 and above, Fig. 1c) are incrementally displaced by $\delta\mathbf{s}$ along the direction of shear $\boldsymbol{\eta}_1$-$[\bar{1}\bar{1}26]$, followed by structure optimization to obtain the GSFE γ-line as a function of the imposed slip displacement $\mathbf{s}$. The difference between the classical and RC γ-lines lie in the degrees of freedom allowed in each structure optimization step. In the classical method, all atoms are fixed in the in-plane directions within the slip/twin plane and atomic displacements are generally only allowed in the slip/twin plane normal direction. In the RC method, only the atoms immediately above and below the twinning plane (layer 8 and 9) are fixed in the twinning $\boldsymbol{\eta}_1$-direction and all other degrees of freedom are optimized (Fig. 1d and see Ref. [30]). For the fully periodic tilt supercell, the incremental slip is introduced by adding $\delta\mathbf{s}$ to the supercell vector in the slip direction, followed by structure optimizations with the same prescribed degrees of freedoms as that in the slab–vacuum supercell. Since the applied displacement $\delta\mathbf{s}$ creates slip discontinuity between two atom layers and does not predetermine the resulting nucleation types, (dislocation or twin), we refer $\delta\mathbf{s}$ as *slip* along $\boldsymbol{\eta}_1$ in the twinning $\mathbf{K}_1$-plane below, similar to that used by J. R. Rice [37] (quite often, one may insist the word "shear" to describe $\delta\mathbf{s}$, as slip might be reserved for dislocation processes and not rightful for twinning. As we showed previously [30] and below, nucleation of twinning and dislocation can be described within the same generalized Peierls framework and thus "slip" is entirely appropriate).

2.2. Supercells for GSFE calculations in DFT

In the DFT calculations, we consider 4 configurations: Mg_{72}, $Mg_{71}Y$, $Mg_{70}Y_2$ and $Mg_{85}Y_3$ (Fig. 2). The first 3 configurations use a slab–vacuum supercell containing an HCP lattice with supercell vectors $\mathbf{c}_1 = [11\bar{2}6]$, $\mathbf{c}_2 = [1\bar{1}00]$, and $\mathbf{c}_3$ in the normal direction of the $\mathbf{K}_1$-$(11\bar{2}1)$ twinning plane. The supercell vector $\mathbf{c}_1$ is along the direction of shear $\boldsymbol{\eta}_1$, $\mathbf{c}_2$ is in the normal of the plane of shear [8], while $\mathbf{c}_3$ is extended to include a total of 36 $(11\bar{2}1)$ atom-layers. Periodic boundary conditions (PBCs) are imposed in all directions and a vacuum layer of 15 Å is added in the $\mathbf{c}_3$ direction to isolate image interactions. The last configuration, $Mg_{85}Y_3$, is a periodic supercell with $\mathbf{c}_1 = [11\bar{2}6]$, $\mathbf{c}_2 = 2[1\bar{1}00]$ and $\mathbf{c}_3 = [55\,\overline{10}\,3]$. This supercell contains 22 $(11\bar{2}1)$ atom-layers and no vacuum layer is introduced. Supercell Mg_{72}, $Mg_{71}Y$ and $Mg_{70}Y_2$ contain 72

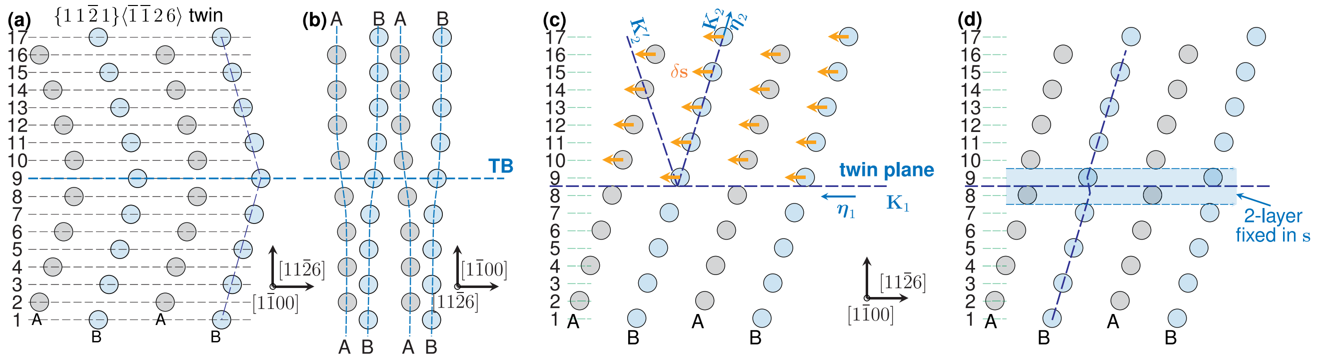

Fig. 1. The $\{11\bar{2}1\}\langle\bar{1}\bar{1}26\rangle$ twin structure in HCP Mg and the reduced-constraint slip method. (a, b) The twin structure calculated in DFT for pure Mg viewed in 2 directions. The plane of shear is $(1\bar{1}00)$ and has an ⋯ABAB⋯ stacking sequence. (c) Atoms above the twin plane are incrementally displaced by $\delta\mathbf{s}$ in the twinning direction. (d) The displaced structure is optimized with only two layers of atoms above and below the twin plane (layer 8 and 9) fixed in the $\mathbf{s}$ direction and all other degrees of freedom fully relaxed.

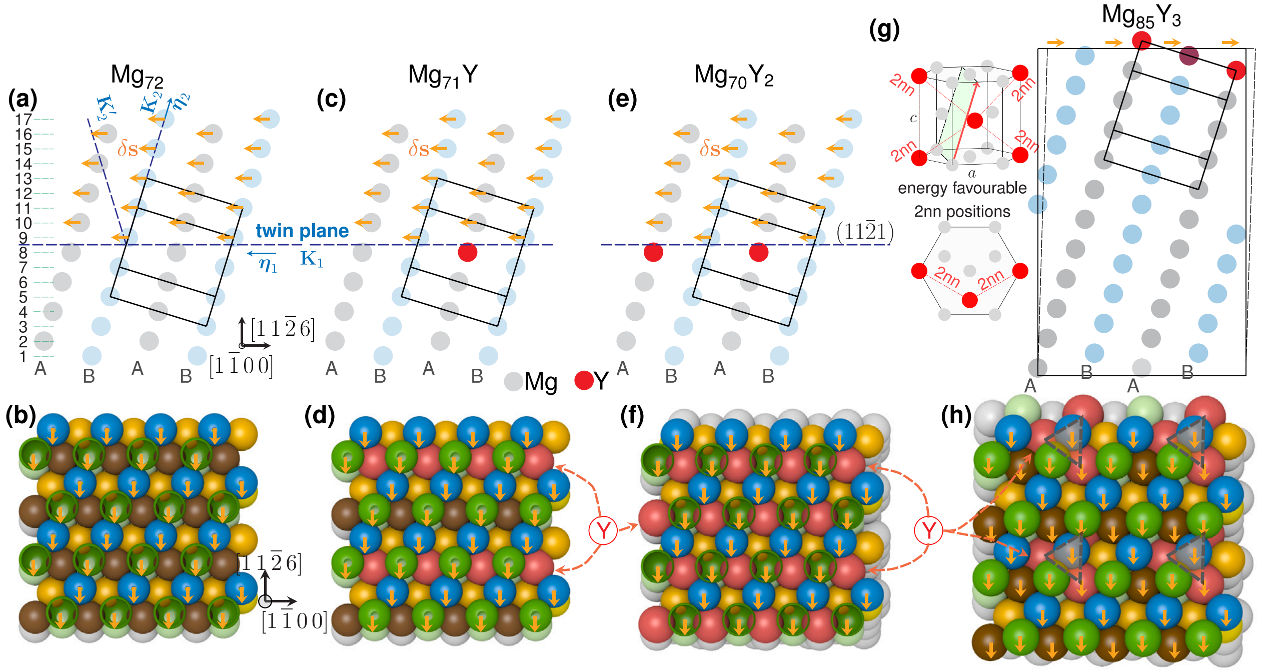

Fig. 2. The supercells for calculating the γ_{rc}-lines in the $[\bar{1}\bar{1}26]$ direction on the $(11\bar{2}1)$ plane in HCP Mg and Mg with Y solutes. (a, b) Supercell for Pure Mg. (c, d) Mg with a single Y solute in the supercell. (e, f) Mg with 2 Y solutes on a $(11\bar{2}1)$ plane in the supercell. (g, h) Mg with 3 Y solutes at energy favourable 2nn positions indicated by the grey triangles [38]. The yellow arrows indicate the incremental slip step δs in the direction of shear $\boldsymbol{\eta}_1 = [\bar{1}\bar{1}26]/3$. In (b, d, f), some atoms are drawn with half-spheres to illustrate the contacts among different $(11\bar{2}1)$ atom-layers and the corrugated $(11\bar{2}1)$ atomic planes. In the bottom row figures, atom colours are chosen based on their distance in the viewing direction to reveal the corrugated $(11\bar{2}1)$ planes. (For interpretation of the references to colour in this figure legend, the reader is referred to the web version of this article.)

lattice points/atoms each. Mg_{72} contains 72 Mg atoms, $Mg_{71}Y$ and $Mg_{70}Y_2$ have one and two Mg atoms replaced by Y solutes near the twining plane (Fig. 2c–f). The PBCs introduce image interactions in the in-plane directions, effectively creating Y solutes segregated at the 4th nearest neighbouring (nn) positions in $Mg_{71}Y$ and at the 4th and 5th nn positions in $Mg_{70}Y_2$. DFT calculations show that the pair-interaction energies are slightly negative or nearly zero at these nn positions (see Ref. [39]). $Mg_{71}Y$ and $Mg_{70}Y_2$ thus represent configurations with some local solute segregation due to *random* solute fluctuations and localized shear (slip) occurs at these solute fluctuations. Nucleation in the truly random solute configurations under stresses are simulated in separate atomistic simulations of mode-II loaded cracks (see below). Lastly, $Mg_{85}Y_3$ contains 88 atoms and is constructed with 3 Y solutes placed at the energetically favourable 2nn positions, which is consistent with the solute short range ordering (SRO) present in Mg–RE experiments [38,40–43] and DFT calculations [39,44] (Fig. 2g,h). In this case, incremental slip δs is realized using the tilt-cell method, i.e., by adding an incremental slip $\delta\mathbf{s}$ to the supercell vector $\mathbf{c}_3$, which tilts the supercell in the $\mathbf{c}_1$ slip direction, followed by structure optimization with 2 $(11\bar{2}1)$ atom-layers fixed in the slip direction (Fig. 2i, see Refs. [6,45–47] for details). We emphasize that the Y-solutes are placed near the slip/twin planes, since nucleation typically occurs at local favourable sites. Therefore, the number of Y solutes in $Mg_{71}Y$, $Mg_{70}Y_2$ and $Mg_{85}Y_3$ has no direct association with Y solute concentrations in experiments. Furthermore, we also calculate the GSFE of $Mg_{70}Al_2$ (Y replaced by Al) for comparison; there is no experimental observation of $\{11\bar{2}1\}\langle\bar{1}\bar{1}26\rangle$ twin in this well-developed alloy system.

2.3. Density functional theory calculations

The GSFE γ-lines and associated atom displacements are calculated using first-principles density functional theory (DFT) calculations as implemented in the Vienna *ab initio* Simulation Package (VASP [48,49]). In DFT, the exchange and correlation interactions are described

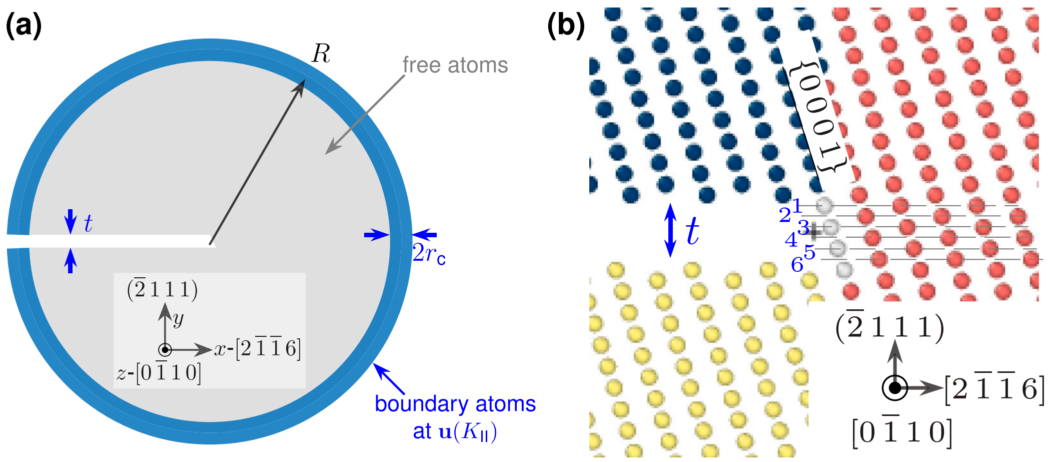

Fig. 3. The semi-infinite crack model and crack tip structure. (a) Schematics of the cylindrical simulation cell of radius R and boundary thickness $2r_c$. (b) The crack-tip atomic structure. Six $(\bar{2}\,1\,1\,1)$-plane atom layers are removed to create the blunted crack. The blunted crack-tip is terminated along the low-energy $(0\,0\,0\,\bar{1})$ plane (white atoms). Interactions between atoms located within $2r_c \approx 15.3$ Å from the upper and lower crack surfaces (atoms coloured dark green and yellow) are cancelled to prevent crack closure, creating traction-free crack surfaces. (For interpretation of the references to colour in this figure legend, the reader is referred to the web version of this article.)

using the generalized gradient approximation (GGA) functionals in the Perdew–Burke–Ernzerhof (PBE) form [50]. The core electrons are replaced by the projector augmented wave (PAW [51]) pseudopotentials. The valence states are $3s^2$, $3s^2 3p^1$ and $4s^2 4p^6 5s^2 4d^1$ for Mg, Al and Y, respectively. A cutoff energy of 520 eV is used for the plane-wave basis set and a first-order Methfessel–Paxton method [52] with a width of 0.1 eV is used to smooth the partial electron occupancies. The Monkhorst–Pack k-point mesh [53] is used to sample the Brillouin zone with a linear k-point spacing of ~0.2 Å^{-1}. Convergence is assumed when the total energy variation drops below 10^{-5} eV.

2.4. Twin nucleation and growth at crack-tips in Mg, MgY and MgAl

To complement the DFT results, we study the $\{1\,1\,\bar{2}\,1\}\langle\bar{1}\,\bar{1}\,2\,6\rangle$ twin nucleation and growth in pure Mg and Mg with random Y or Al solutes using atomistic simulations. We simulate local stress concentrations using a slightly blunted, semi-infinite crack under mode-II loadings. The crack-tip produces a general stress concentration with localized shear/slip deformation, which is also similar to that at triple junctions of sliding GBs [27,54], at dislocation pile-ups near GBs, etc. This approach is commonly used in predicting twinning and dislocation emission in FCC and BCC structures [25–27,30,55].

Specifically, a crack is constructed with a $(\bar{2}\,1\,1\,1)[0\,\bar{1}\,1\,0]$ orientation, where $(\bar{2}\,1\,1\,1)$ and $[0\,\bar{1}\,1\,0]$ are the crack plane and crack front direction, respectively (Fig. 3). The selected crack orientation and loading mode are favourable for the $\{1\,1\,\bar{2}\,1\}\langle\bar{1}\,\bar{1}\,2\,6\rangle$ twin nucleation. The crack system consists of a cylinder of radius $R \approx 200$ Å, and with its axis aligned in the z-axis and the crack plane parallel to the $x-z$ plane (Fig. 3a). Periodic boundary conditions are applied in the z direction. The thickness of the cylinder, i.e., the crack front length, is ~5.5 Å (1 periodic spacing) for pure Mg and ~45 Å (8 periodic spacings) for the alloy. Although we are only concerned with quasi-2D crack response in pure Mg, MgY and MgAl alloys, a thicker crack model is required for the alloy for at least two reasons. First, when the model thickness is not significantly larger than the average solute spacing, the effective solute concentration along the z-direction will be larger than the apparent volumetric concentration due to the periodic boundary conditions in z. When the effective concentration increases beyond the solubility limit, the HCP structure may become unstable (as exhibited by the current XMEAM interatomic potential and see phase diagram for the binary MgY system [56]). Second, crack tip responses (nucleation events) can be quite sensitive to near-tip solute distributions [57]. Increasing crack front length offers wider sampling opportunities and thus makes simulation results less sensitive to change of solute distributions.

Furthermore, the crack-tip is slightly blunted, since the initial nucleation and later lateral growth of a twin lamella may require sequential nucleations of twinning disconnections on adjacent twinning planes [55,58]. In practice, the blunted crack is created by removing six $(\bar{2}\,1\,1\,1)$-plane atom layers terminated along a low-energy $(0\,0\,0\,\bar{1})$ plane (white atoms in Fig. 3b). The free surface of the blunted crack tip readily provides nucleation sites for such twinning disconnections which are not available at a sharp crack tip under mode-II loading. Furthermore, the traction-free crack surface is modelled by cancelling the interactions between atoms located within $2r_c \approx 15.3$ Å ($2\times$ the cut off distance of the interatomic potential) from the upper and lower crack surfaces (atoms coloured dark green and yellow in Fig. 3b), which also prevents potential crack closure under mode-II loadings. The above treatment is a common approach used in atomistic simulations of twin nucleation in FCC and BCC structures [25,30,58].

Atoms within $2r_c$ from the outer cylinder surface are treated as boundary atoms and all others as free atoms (Fig. 3a). The crack is loaded by incrementally displacing the free/boundary atoms according to the asymptotic anisotropic elastic solution of a semi-infinite crack under plain strain conditions [59], i.e.,

$$\mathbf{u} = \sqrt{\frac{2}{\pi}}\,\Re\left\{\mathbf{A}\left\langle\sqrt{r\cos\theta + p_\alpha \sin\theta}\right\rangle\mathbf{B}^{-1}\right\}\mathbf{K}, \tag{1}$$

where $\mathbf{A}$, $\mathbf{B}$, p_α are the Stroh matrices and eigenvalues, r and θ are the polar coordinate centred at the crack tip, $\langle\cdot\rangle$ denotes a diagonal matrix and $\mathbf{K}$ is the stress intensity factor (for details, see Ref. [59]).

The crack is first directly loaded to $K_{\mathrm{II0}} = 0.080$ MPa$\sqrt{\mathrm{m}}$ by displacing all atoms according to the elastic solution $\mathbf{u}(K_{\mathrm{II0}})$. Below this threshold stress intensity factor (SIF), the crack system restores to the initial state upon unloading. The applied load is then increased incrementally with $\Delta K_{\mathrm{II}} = 0.005$ MPa$\sqrt{\mathrm{m}}$ by displacing only the boundary atoms to $\mathbf{u}(K_{\mathrm{II0}} + n\Delta K_{\mathrm{II}})$, where n is the incremental step. Between each load increment, the structure is optimized with boundary atoms fixed at the corresponding $\mathbf{u}(K_{\mathrm{II}})$. During each structure optimization, convergence is assumed when the atomic forces fall below 10^{-9} eV/Å on the free atoms.

To demonstrate the distinct effects of Y and Al solutes on the $\{1\,1\,\bar{2}\,1\}\langle\bar{1}\,\bar{1}\,2\,6\rangle$ twin nucleation, we study the crack-tip responses under loading in pure Mg, Mg–1.5at.%Y, Mg–3at.%Y and Mg–3at.%Al. The $\{1\,1\,\bar{2}\,1\}\langle\bar{1}\,\bar{1}\,2\,6\rangle$ twin is prevalent and absent in the last two alloys (i.e., Mg–10wt.%Y and Mg–4.5wt.%Al) during room-temperature deformation experiments [16,17]. In the alloys, Y and Al solutes are distributed randomly and 8 samples with different random seeds are generated and simulated.

In the mode-II loaded simulations, the crack tip will eventually reach elastic instability (localized slip between two layers or more) and emit a dislocation or form a twin nucleus at critical loadings $K_{\mathrm{IIe,\ Sim}}$. Alternatively, the critical loading may also be estimated using the Rice criterion with inputs of the unstable SFE γ_{us}, elastic constants [37] and crack orientation as

$$K_{\mathrm{IIe,Rice}} = \sqrt{\gamma_{\mathrm{us}}(\mathbf{\Lambda}^{-1})_{11}}, \tag{2}$$

Here, the unstable SF energy γ_{us} can also be taken as the barrier to nucleate a twin nucleus γ_{utw} if a twin is subsequently formed at the metastable SF position on the γ_{rc}-line [36], and $\Lambda = \frac{1}{2}\Re\{i\mathbf{AB}^{-1}\}$ is a positive definite Hermitian matrix in the Stroh formalism. We shall compare the critical SIF K_{IIe} values from both the direct atomistic simulations and the theoretical model.

2.5. Atomistic simulations using XMEAM potentials for MgY and MgAl

Atomistic simulations are carried out using the Large-scale Atomic/Molecular Massively Parallel Simulator (LAMMPS [60]). Interatomic interactions are described by new potentials for MgY and MgAl [61]. These potentials accurately reproduce a wide range of lattice and defect properties for the MgY and MgAl binary systems, including the Y–Y and Al–Al pair interaction energies and the $\{11\bar{2}1\}\langle\bar{1}\bar{1}26\rangle\gamma$-lines in agreement with DFT. Below we briefly describe its key features and compare relevant properties for the current study with DFT. Details of the potential development will be reported separately, but the potential can be accessed immediately [61].

3. Results

3.1. GSFEs and atom displacements in pure Mg

We first compare the γ-lines calculated using the classical and RC methods. Since $\{11\bar{2}1\}\langle\bar{1}\bar{1}2\bar{6}\rangle$ deformation twinning was observed in previous MD simulations of pure Mg using two EAM interatomic potentials [23,62,63], we also benchmark these two potentials against the γ-lines based on DFT. Fig. 4 shows the classical and RC γ-lines in pure Mg calculated using DFT, XMEAM, the EAM potential by Sun et al. [62] and the EAM potential by Liu et al. [63]. On the *classical* $\{11\bar{2}1\}\langle\bar{1}\bar{1}26\rangle$ γ-lines, all four models show rapid increases of GSFE with increasing slip $\mathbf{s}$. No metastable SF is seen in any model even after the slip distance $\mathbf{s}$ well-passes the twinning Burgers vector $\mathbf{b}_{\mathrm{t}} = \dfrac{1}{4(c/a)^2+1}\mathbf{b} = 0.0869\mathbf{b}$ [1], where $\mathbf{b} = [\bar{1}\bar{1}2\bar{6}]/3$. The rapid increase of the GSFE on this plane is also higher than the GSFE for $\langle\mathbf{c}+\mathbf{a}\rangle$ slips (~0.2–0.3 J/m^2) on pyramidal planes [6], suggesting that nucleation of dislocation or twin on the $\{11\bar{2}1\}$ plane encounters a higher energy barrier and is highly unfavourable compared to $\langle\mathbf{c}+\mathbf{a}\rangle$ dislocation nucleations and slips in Mg.

Fig. 4b shows the respective γ_{rc}-lines calculated by the RC method. In all the models, the RC method reduces the GSFE by more than 50% from their respective classical γ-lines. This is not surprising, since the slip path along $\langle\bar{1}\bar{1}2\bar{6}\rangle$ is corrugated on the $\{11\bar{2}1\}$ plane and shuffle displacements are expected along $\langle1\bar{1}00\rangle$ (Fig. 2a). For example, when the blue atom-layer is displaced in the $\boldsymbol{\eta}_1$ direction, it will encounter the brown atom-layer, resulting in shuffle displacements in the other 2 directions perpendicular to $\boldsymbol{\eta}_1$. In the classical γ-line, such shuffle displacements are constrained (Fig. 4c) while the RC method removes these constraints completely (Fig. 4d). The two EAM potentials possess metastable SFs at $\mathbf{s} \approx 0.07\mathbf{b}$ and $\mathbf{s} \approx 0.09\mathbf{b}$ close to the twinning Burgers vector $\mathbf{b}_{\mathrm{t}}$. Their unstable SFE γ_{us} are 0.137 and 0.213 J/m^2, which are 63% and 42% lower than the DFT value. These two EAM potentials significantly underestimate the barrier to activating dislocation slip/twinning on the $\{11\bar{2}1\}$ plane and thus cannot provide quantitative predictions on the dislocation/twin nucleation conditions. In contrast, the XMEAM has nearly the same γ_{rc}-line profile as that in DFT; both have no metastable SF near $\mathbf{s} = \mathbf{b}_{\mathrm{t}}$.

Fig. 5 shows the atomic displacements of all four models. The structures in the two EAM potentials are chosen at their metastable SF positions, while that in DFT and XMEAM are at slips near $\mathbf{b}_{\mathrm{t}}$. Along the γ_{rc} path, all models exhibit appreciable atom displacements in the $\mathbf{K}_1$-plane normal direction; the displacements are localized above and below the slip plane (between layer 8 and 9). In addition, shuffle displacements are seen in the $\langle1\bar{1}00\rangle$ direction (green arrows in Fig. 5), as dictated by the corrugated atomic structure of the $\{11\bar{2}1\}$ plane. The shuffle displacements propagate away from the slip plane and their magnitudes vary among the models. The overall shuffle displacements are smallest in DFT, and largest in the two EAM potentials. In particular, a 4-layer twin is spontaneously formed in EAM-Sun during RC slip (Fig. 5c). All the slipped structures are then further optimized by removing all constraints to examine their stability. In DFT and XMEAM, the structures are unstable and revert to the original perfect lattice, consistent with the lack of metastable SFs on their respective γ_{rc}-lines (Fig. 4b). On the other hand, the slipped structures are stable in EAM-Sun and EAM-Liu; the structure further grows to a 4-layer twin in EAM-Liu (Fig. 5f). We note that the $\{11\bar{2}1\}\langle\bar{1}\bar{1}26\rangle$ twin was observed in MD simulations of pure Mg using these two EAM potentials [23]; the easy activation of this twin mode is a result of the deficiency of the underlying interatomic potentials (substantially lower γ_{us} and the presence of the metastable SF). Furthermore, the previous MD results are not consistent with broad experiments where neither dislocation slip nor twinning is normally activated on this plane in quasi-static deformation of pure Mg.

For the current $\{11\bar{2}1\}\langle\bar{1}\bar{1}26\rangle$ twin in Mg, DFT calculations here show that the slipped structure at $\mathbf{s} = \mathbf{b}_{\mathrm{t}}$ is not even metastable, which is similar to that of the $\{112\}\langle\bar{1}\bar{1}1\rangle$ twin in BCC W and Mo [30]. For such cases, the generalized planar fault energy (GPFE [25,31,32]) can be employed to give an upper bound of the twin nucleation barrier. Fig. 6 shows the GPFE curves computed by DFT and XMEAM. Both GPFE curves have similar profiles with no obvious meta-stable SFs. To form a three-layer twin, the barriers from DFT and XMEAM are 0.397 J/m^2 and 0.425 J/m^2, respectively. While the GPFE curves suggest that a three-layer twin is not stable, nucleation may still be possible under large applied shear loadings such as at blunted crack-tips, as demonstrated in MD simulations below. Nonetheless, the GPFE curves suggest that $\{11\bar{2}1\}\langle\bar{1}\bar{1}26\rangle$ twinning encounters high energy barriers in pure Mg.

3.2. GSFEs and atom displacements in random MgY and MgAl alloys

Since the EAM-Sun and EAM-Liu potentials do not have accurate γ_{rc}-lines and cannot quantitatively predict the onset of twinning, we focus on the results of DFT and XMEAM below. Fig. 7 shows the respective classical and RC γ-lines in Mg$_{71}$Y, Mg$_{70}$Y$_2$ and Mg$_{70}$Al$_2$. The XMEAM potential for MgY again exhibits γ-lines close to that of DFT. In both structures, the γ_{rc}-lines are much lower than the corresponding γ-lines due to the reduced constraints allowing shuffle displacements. Mg$_{71}$Y has γ_{rc}-line profiles similar to that in pure Mg; both γ_{rc}-lines increase monotonically without any metastable SF at slips close to the twinning Burgers vector $\mathbf{b}_{\mathrm{t}}$. In contrast, Mg$_{70}$Y$_2$ in DFT first reaches a peak $\gamma_{\mathrm{utw}} \approx 0.319$ J/m^2 at $\mathbf{s} \approx 0.075\mathbf{b}$, followed by an energy valley/a metastable SF $\gamma_{2\mathrm{tw}}$ of 0.299 J/m^2 at slip $\mathbf{s} \approx 0.08\mathbf{b}$ close to $\mathbf{b}_{\mathrm{t}}$ [8]. The XMEAM also has a meta-stable SF at $\mathbf{s} \approx \mathbf{b}_{\mathrm{t}}$ in Mg$_{70}$Y$_2$, in agreement with DFT. Furthermore, both DFT and XMEAM do not show a meta-stable SF on the γ_{rc}-lines in Mg$_{70}$Al$_2$, demonstrating the distinct effects of Y and Al solutes in Mg. On the other hand, the metastable SFs in EAM-Sun and EAM-Liu are artefacts for pure Mg, which further highlights the complexities and challenges in fitting accurate interatomic potentials for HCP systems.

The presence of the metastable SFs are dictated by the shuffle displacements in the $\langle1\bar{1}00\rangle$ direction (Fig. 7d,e), as expected from the corrugated slip path on the $\mathbf{K}_1$ twinning plane (Fig. 2b). The amount

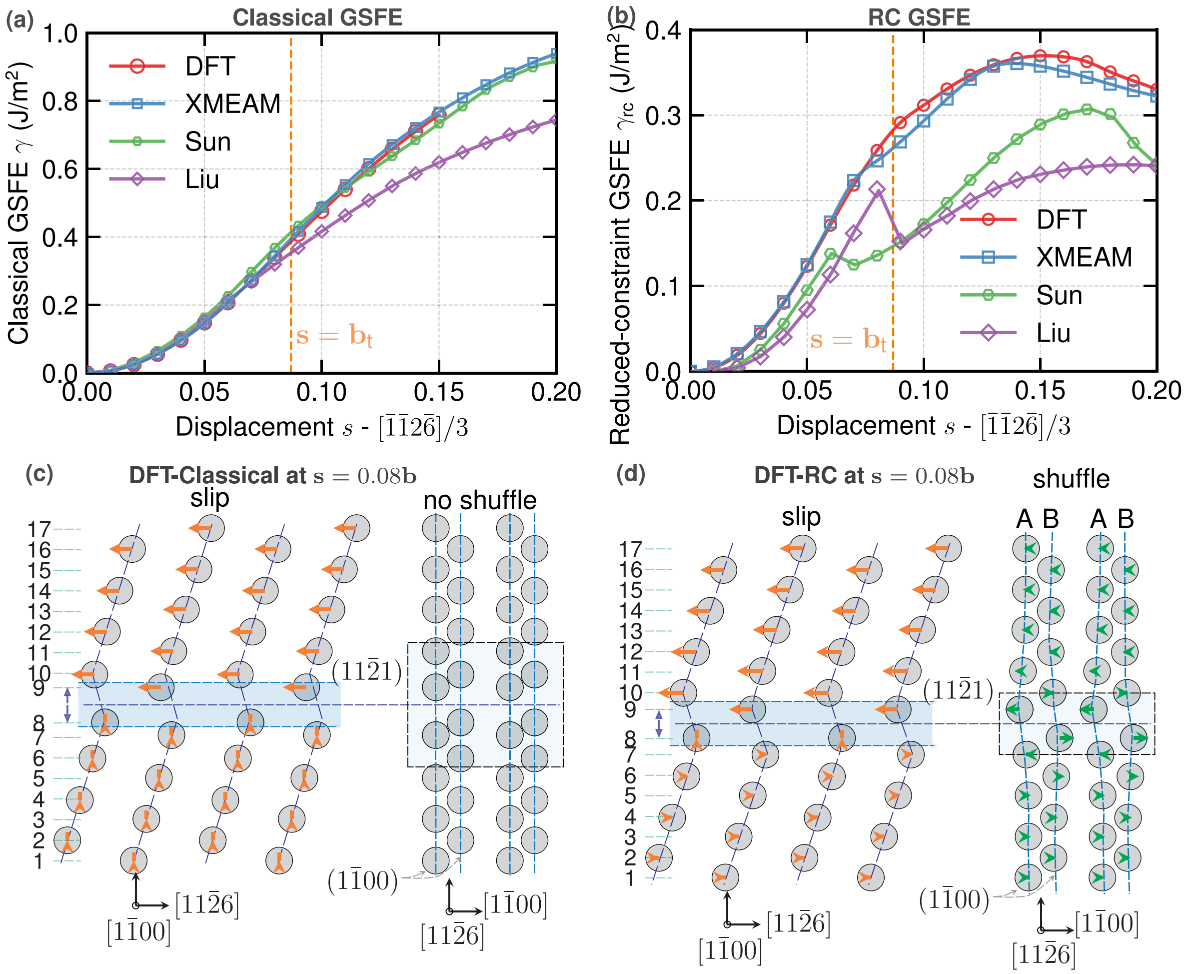

Fig. 4. The $\{1\,1\,\bar{2}\,1\}\langle\bar{1}\,\bar{1}\,2\,6\rangle$ GSFE γ-lines and slipped structures calculated by DFT, XMEAM, EAM-Sun [62] and EAM-Liu [63] for HCP Mg. (a) The classical γ-lines. (b) The reduced-constraint $\gamma_{\rm rc}$-lines. (c, d) The atomic structures and displacements at the critical slip $\mathbf{s} \approx \mathbf{b}_t \approx 0.08\mathbf{b}$ calculated by the classical and RC methods in DFT. In (a, b), the orange dashed lines mark the critical slip corresponding to the twinning Burgers vector $\mathbf{b}_t$. In (c, d), the orange and green arrows (magnified by 2 times) are the displacements in the slip and shuffle directions at $\mathbf{s} \approx \mathbf{b}_t$. (For interpretation of the references to colour in this figure legend, the reader is referred to the web version of this article.)

of shuffle depends on the electronic structure/interatomic bondings and thus varies among the elemental HCP metals or with local solute species in their alloys. In DFT and XMEAM for pure Mg, the shuffle displacements are rather small compared to that required for the twin formation (cf. Fig. 8a and d). In contrast, $Mg_{71}Y$ and $Mg_{70}Y_2$ have their shuffle displacements enhanced in the $\langle 1\,\bar{1}\,0\,0\rangle$ direction by Y solutes (cf. Fig. 8d, e and f). In particular, $Mg_{70}Y_2$ has substantial atomic shuffle in $\langle 1\,\bar{1}\,0\,0\rangle$ among multiple $(1\,1\,\bar{2}\,1)$ planes above and below the slip plane. For example, the shuffle displacements are ~0.42 and −0.59 Å in layer 8 and 7 (Figs. 7c and 8f), which are close to ±0.465 Å to reverse the asymmetry of the $(1\,\bar{1}\,0\,0)$ A and B atom-planes [8] and satisfy the crystallographic requirement for the formation of the $\{1\,1\,\bar{2}\,1\}$-twin. The Y-enhanced shuffle is not surprising since Y has a large misfit volume in Mg ($\Delta V/V_0 \approx 0.6$ [39]) and thus induces stronger repulsion along the RC slip path (Fig. 2f). In $Mg_{70}Al_2$, both DFT and XMEAM show that the shuffle displacements are rather small and similar to that in pure Mg; no twin embryo is formed along the RC slip path (Fig. 7f,g), corroborating the lack of meta-stable SF on their $\gamma_{\rm rc}$-lines.

Similar to that in pure Mg, the slipped structures in $Mg_{71}Y$ and $Mg_{70}Al_2$ are unstable when optimized with all constraints removed; these structures fall back to the initial HCP structure (Fig. 8d to a, e to b), consistent with its $\gamma_{\rm rc}$-line. In contrast, the structure in $Mg_{70}Y_2$ at the *critical* slip $|\mathbf{s}| = 0.078|\mathbf{b}| \approx 0.84$ Å spontaneously transforms into a $\{1\,1\,\bar{2}\,1\}$ twin embryo of 7 atom-layers during constraint-free optimization (Fig. 7d). Within the twin-embryo, the *shear deformation* follows the homogeneous twin shear $s = a/c$, as dictated by the symmetry requirement of the $(11\bar{2}1)$ twin [8]. Neither of the 2 twin boundaries (TBs) enclosing the twin embryo lands on the atom layer with Y solutes. This is not surprising either, since the Y-enhanced shuffling initiates at the slip plane with Y and spreads in opposite directions normal to the slip plane. The constraint-free optimization further decreases the excessive energy to 0.274 J/m^2, slightly higher than $2 \times \gamma_{(11\bar{2}1)} = 245$ mJ/m^2 of the TB energy in *pure* Mg [20]. This small difference may arise from interactions of the 2 TBs and the presence of the Y solutes close to the TB in the current supercell. Furthermore, the XMEAM for MgY and MgAl exhibit similar shuffle displacements and twin formation as in DFT (cf. Fig. 7d and e, f and g), which demonstrates their appropriateness for the atomistic simulations in Section 3.5.

3.3. GSFE and slipped structures in MgY alloys with random Y solutes

While the above reduced-constraint GSFE and atomic structures clearly demonstrate the effectiveness/ineffectiveness of Y/Al solutes on activating the $\{1\,1\,\bar{2}\,1\}\langle\bar{1}\,\bar{1}\,2\,6\rangle$ twin, the supercells are still special since the solutes are strategically placed around the slip plane. To examine the GSFE and slipped structures at random solute environment (perhaps closer to some experiments), we create a larger supercell with 3at.% Y randomly distributed (Fig. 9a). Six GSFE $\gamma_{\rm rc}$-lines are calculated using the XMEAM potential for MgY (Fig. 9h). Among them, meta-stable points are seen in four $\gamma_{\rm rc}$-lines where Y is located above or below the

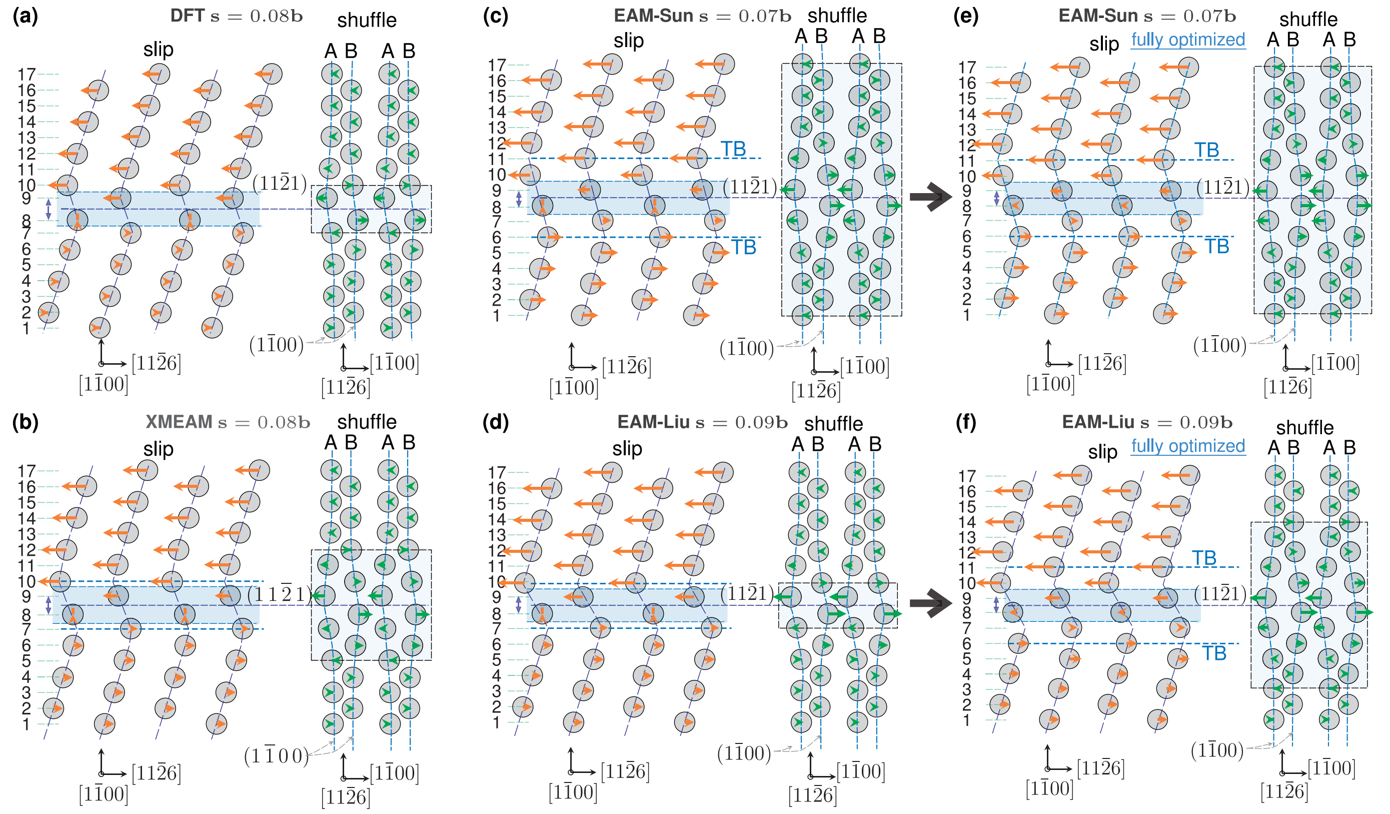

Fig. 5. The atomic structures slipped in the $\langle\bar{1}\bar{1}26\rangle$ direction on the $\{11\bar{2}1\}$ plane calculated by the reduced constraint method for Mg. (a, b) The structure at $\mathbf{s} \approx \mathbf{b}_t = 0.08\mathbf{b}$ in DFT and XMEAM. (c) The structure, i.e., a 4-layer twin spontaneously formed at the metastable SF $\mathbf{s} = 0.07\mathbf{b}$ in EAM-Sun [62] (Fig. 4b). (d) The structure at the metastable SF $\mathbf{s} = 0.09\mathbf{b}$ in EAM-Liu [63] (Fig. 4b). (e, f) The twin structure from that in (c) and (d) after constraint-free optimization. The orange and green arrows (magnified by 2 times) are the displacements in the slip and shuffle directions at $\mathbf{s} = \mathbf{b}_t$. The shuffle displacements are largest in EAM-Sun and EAM-Liu. (For interpretation of the references to colour in this figure legend, the reader is referred to the web version of this article.)

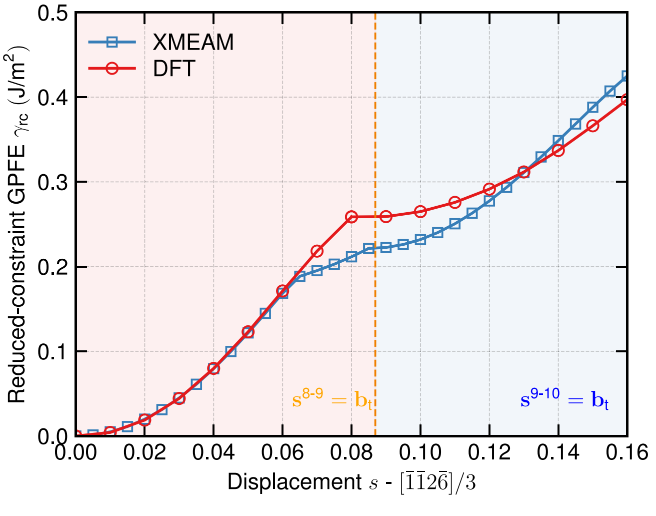

Fig. 6. The generalized planar fault energy (GPFE) in the $[\bar{1}\bar{1}2\bar{6}]$ direction on the $(11\bar{2}1)$ plane computed by DFT and XMEAM for Mg. The GPFE curves are computed by first incrementally adding $\delta\mathbf{s}$ along the slip plane between atom layer 8 and 9 (Fig. 1d) and calculating the corresponding γ_{rc} up to $\mathbf{s} = \mathbf{b}_t$. The second slip $\delta\mathbf{s}$ is added along the slip plane between atom layer 9 and 10, followed by calculating the corresponding γ_{rc} up to $\mathbf{s} = \mathbf{b}_t$ while holding the slip between layer 8 and 9 at $\mathbf{b}_t$.

chosen slip plane (Slip plane 2, 3, 4, 5), while no meta-stable point is seen in the other two slip planes with no Y nearby (Slip plane 1 and 6). Similar to the cases shown in Fig. 7, the $\{11\bar{2}1\}$ twin is spontaneously formed in the cases with the meta-stable point (Fig. 9c,d,e,f), and no twin is formed in the rest (Fig. 9b,g). This further demonstrates the generality of the Y-enabled twinning mechanism and its operation in random solute environments.

3.4. GSFEs and atom displacements in MgY alloys with SRO

The combination of slip in $[\bar{1}\bar{1}2\bar{6}]$ and Y-enhanced shuffling in $\langle 1\bar{1}00\rangle$ provides the required atomic displacements for the $\{11\bar{2}1\}$ twin formation (Fig. 1a,b). However, the present $Mg_{70}Y_2$ supercell contains a layer of Y solutes which can only be realized *locally* under random solute fluctuations. Such a configuration can be statistically important with increasing Y solute concentrations. On the other hand, Y solutes in SRO may also facilitate the twin formation. In general, SRO exists in solid solution alloys at any finite temperatures, as dictated by thermodynamics and independent of whether it can be detected or not. SRO is widely reported in Mg–RE alloys. The energetically favourable 2nn-SRO configuration has a zig-zag atomic arrangement when viewed in the $\langle \mathbf{c}\rangle$ axis (Fig. 2g), which is consistent with HAADF-STEM images showing Y-enriched regions in Mg–2at.%Y after homogenization and ageing [38,40,42], HAADF-STEM images showing different Y occupations in Mg–11wt.%Y after homogenization and ageing [38], as well as observations in MgGd [43] and MgNd [41]. In addition, DFT calculations show that the 2nn-SRO configuration has the lowest energy among a broad range of configurations including ordered, random and segregation structures [44]. It is also the precursor to the formation of solute clusters/G. P. Zone and following β' (Mg_7Y) and β'' precipitates in the MgY system. Given the widely reported SRO in experiments and computational results, we next examine the γ_{rc}-line in $Mg_{85}Y_3$ (Fig. 10). The γ_{rc}-line has a similar profile as that in Mg and $Mg_{71}Y$; no metastable SF is present. Y-solutes again increase the γ_{rc}-line relative to that in pure

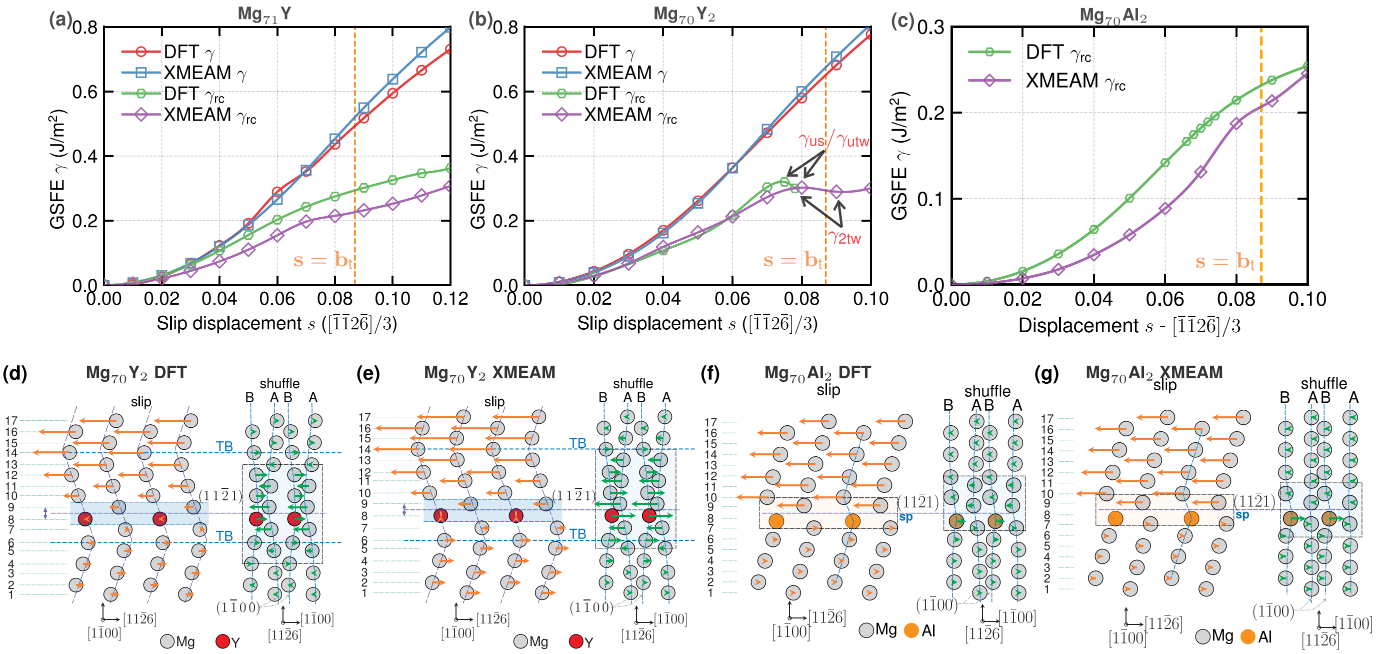

Fig. 7. The classical GSFE γ-lines, reduced-constraint γ_{rc}-lines and atomic structures at the metastable SF in MgY and MgAl alloys calculated by DFT and XMEAM. (a, b, c) The γ and γ_{rc}-lines in the $\boldsymbol{\eta}_1 - [\bar{1}\bar{1}2\bar{6}]$ direction on the $(11\bar{2}1)$ plane in $Mg_{71}Y$, $Mg_{70}Y_2$ and $Mg_{70}Al_2$. In $Mg_{70}Y_2$, a metastable SF (γ_{2tw}) is present in the γ_{rc}-lines at the critical slip $\mathbf{s} \approx 0.08\mathbf{b}$. (d, e) The optimized atomic structure at slip $\mathbf{s} = 0.08\mathbf{b}$ in $Mg_{70}Y_2$. A 7-layer twin embryo is formed with slip and shuffle displacements reversing the asymmetry of the $(1\bar{1}00)$ planes. (f, g) The optimized atomic structures at slip $\mathbf{s} = 0.08\mathbf{b}$ in $Mg_{70}Al_2$. No twin embryo is formed and the shuffle displacements are similar to that in pure Mg (Fig. 5a,b). The orange and green arrows (magnified by 2 times) are the atomic displacements in the slip direction and shuffle directions. (For interpretation of the references to colour in this figure legend, the reader is referred to the web version of this article.)

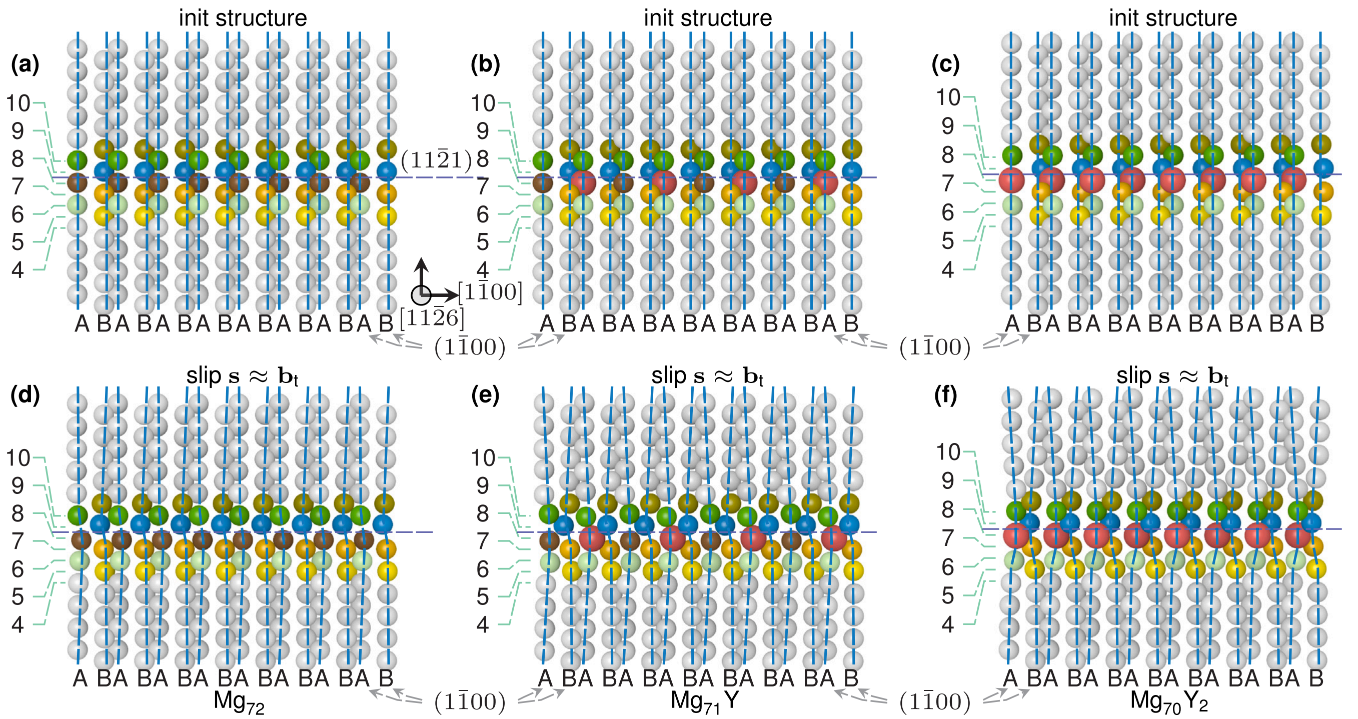

Fig. 8. Atomic structures before and after slip viewed in the $\boldsymbol{\eta}_1 - [\bar{1}\bar{1}2\bar{6}]$ twinning direction calculated in Mg and MgY alloys by DFT. (a, d) Pure Mg. (b, e) $Mg_{71}Y$. (c, f) $Mg_{70}Y_2$. The configurations in (a–c) are the initial fully optimized structures with negligible shuffling displacements. The configurations in (d–f) are the optimized structures with 2 atom-layers constrained in the slip direction at slip $\mathbf{s} \approx 0.08\mathbf{b}$. The blue dashed lines highlight the contoured $(1\bar{1}00)$ planes due to slip. Slip drives shuffling displacements in $\langle 1\bar{1}00 \rangle$ among several atom-layers above and below the slip plane, which are further enhanced by Y solutes in $Mg_{71}Y$ and $Mg_{70}Y_2$. (For interpretation of the references to colour in this figure legend, the reader is referred to the web version of this article.)

Mg; this increase is expected since Y-solutes are placed in the energy-favourable SRO positions and the slip process pulls the Y-solutes out of the SRO configuration.

Furthermore, the 2 atom-layers immediately above and below the slip plane (layer 6 and 7 in Fig. 10e) now contain a mixture of Mg and Y. The RC slip method constrains the relative displacements of all

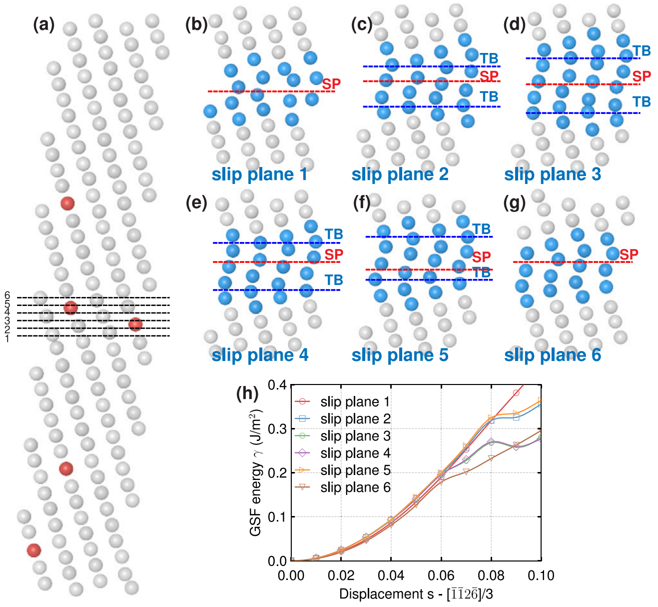

Fig. 9. Supercell, slipped structures and reduced-constraint GSFE γ_{rc}-lines for Mg–3at.%Y with random Y distribution. (a) The initial supercell for Mg–3at.%Y alloy with Y randomly distributed. The dashed lines indicate different slip planes for the γ_{rc} calculations using XMEAM. The red atoms are Y solutes. (b–g) The optimized atomic structures at slip $\mathbf{s} \approx 0.08\mathbf{b}$ along different slip planes. The dashed blue lines and dashed red lines are twin boundaries and slip planes, respectively. (h) The γ_{rc}-lines for the six different slip planes shown in (a). (For interpretation of the references to colour in this figure legend, the reader is referred to the web version of this article.)

atom species in these two layers in the slip direction $\mathbf{s}$, while the Mg and Y atoms should have different amount of slips. The RC slip is thus still over-constrained; atomic strains between different species will arise and are not fully relieved along the slip path. The γ_{rc}-line should be viewed as an upper bound. The current RC slip leads to severe lattice distortions above and below the slip plane in the other 2, constraint-free directions in $\mathrm{Mg}_{85}\mathrm{Y}_3$. In particular, the shuffle displacements in $\langle 1\bar{1}00\rangle$ are even larger than that in $\mathrm{Mg}_{70}\mathrm{Y}_2$ (Fig. 10d), which again severely distorts the $(1\bar{1}00)$ A and B planes above and below the slip plane. The RC slipped structure transforms into a 10-layer twinned structure in subsequent constraint-free optimization (Fig. 10d to f). The final total excessive energy is $\gamma_{2\mathrm{tw}} \approx 0.250$ mJ/m^2, close to the combined energy of two standalone TBs. This transformation occurs via the propagation of the $\langle 1\bar{1}00\rangle$ shuffling from the Y-containing atom layer towards opposite directions, which is similar to that in $\mathrm{Mg}_{70}\mathrm{Y}_2$. The two TBs are thus always located away from the Y-solute layer (Fig. 10b). In the SRO configuration, the XMEAM potential exhibits similar γ_{rc}-line and twinning behaviour as that in DFT. The Y-solutes in the 2nn-SRO configuration can thus facilitate the $\{11\bar{2}1\}\langle\bar{1}\bar{1}26\rangle$ twin nucleation. We emphasize that SRO is not a necessary condition for the activation of this twin, but merely has similar effects as random configurations with some local fluctuations.

The above results demonstrate the Y effects in nucleating the $\{11\bar{2}1\}\langle\bar{1}\bar{1}26\rangle$ twin in Mg. Essentially, localized slips in the twinning direction provide the required atomic displacements to achieve the twinning shear while the shuffle displacements are the natural response of the slip on the corrugated twinning plane. The amount of shuffle is insufficient in pure Mg and Y-solutes increase the shuffle to that required for twin formation as dictated by crystallography. While the presence of Y-solutes slightly increases γ_{rc} relative to that in pure Mg, Y solutes stabilize the structure at the critical slip $\mathbf{s}_{\mathrm{crit}} \approx \mathbf{b}_{\mathrm{t}}$ and enable the twin nucleation. The corresponding energy barrier at $\mathbf{s}_{\mathrm{crit}}$ is $\gamma_{\mathrm{utw}} \approx 0.3$ J/m^2 (Fig. 7b), similar to that for the nucleation of $\langle\mathbf{c}+\mathbf{a}\rangle$ dislocations on the pyramidal I or II planes [6]. Twin nucleation thus becomes an alternative deformation mechanism competitive to dislocation nucleations when shear is localized to a few atom layers, such as at dislocation pile-ups, GB triple junctions or crack tips [5]. Without the Y-solutes, the $\{11\bar{2}1\}$ twin may be nucleated via the multilayer slip mechanism. However, this scenario is unlikely in pure Mg since the corresponding energy barrier is much higher (Fig. 6). All of the above results are also consistent with (i) solution-treated MgY experiments where $\{11\bar{2}1\}$ twinning becomes dominant in alloys with increasing Y/Gd concentration [17,20] and (ii) WE54 experiments where ageing treatment reduces Y solute concentrations and deactivates the $\{11\bar{2}1\}$ twinning [18]. The activation energy barrier γ_{utw} can be further reduced by Y solutes in random alloys with local fluctuations, as examined below.

3.5. Twin nucleation and growth at crack-tips in Mg and random MgY alloys

Fig. 11 shows the crack-tip responses in pure Mg and Mg–3at.%Y. In pure Mg, a basal $\langle\mathbf{a}\rangle$ dislocation is first nucleated at a critical stress intensity factor (SIF) of $K_{\mathrm{IIe,Sim}} = 0.105$ MPa$\sqrt{\mathrm{m}}$ (Fig. 11a), followed by the nucleation of the $\{11\bar{2}1\}\langle\bar{1}\bar{1}26\rangle$ twin at a much higher SIF (Fig. 11d). The twin nucleation occurs by first forming a slip fault at $K_{\mathrm{II}} \approx 0.135$–$0.145$ MPa$\sqrt{\mathrm{m}}$, which qualitatively resembles the slipped structure along the RC path (cf. Fig. 12a–c and d–e). This early slip fault is unstable (and with no hysteresis) upon unloading, which is consistent with the γ_{rc}-line (Fig. 4b). Twin nucleation thus must occur via multilayer-slip, as that in BCC Mo and W [30]. Using the barrier $\gamma_{\mathrm{us}} \approx 0.425$ J/m^2 for forming a 3-layer twin from the GPFE curves (Fig. 6), the critical SIF (Eq. (2)) is $K_{\mathrm{IIe,Rice}} \approx 0.154$ MPa$\sqrt{\mathrm{m}}$, which is close to the $K_{\mathrm{IIe,\ Sim}} \approx 0.145$ when the twin nucleus is formed in the simulation (Fig. 12e). This close agreement is remarkable, but is perhaps a co-incidence, since several complexities are not taken into account in applying the Rice criterion. For example, the effects of surface step [58] and the bluntness of the crack-tip may have strong influences on the critical SIF. The GPFE curve is constructed following a prescribed slip sequence, i.e., first slip between layer 8 and 9 to $\mathbf{b}_{\mathrm{t}}$, followed by between 9 and 10 (Fig. 2d). Such a prescribed slip sequence should be viewed as an upper bound of the energy barrier. At the crack tip, the actual nucleation path may not follow the exact sequence and the true barrier may be lower than that on the GPFE. Further increasing the load to 0.150 MPa$\sqrt{\mathrm{m}}$ drives the nucleation of a pair of twinning disconnections and the formation of a 4 atom-layer twin nucleus (Fig. 12f). In addition, the growth of the twin appears sluggish and requires continuous increase of K_{II}; the twin length grows to 4.7 nm with the applied load increased to 0.160 MPa$\sqrt{\mathrm{m}}$ (Fig. 11g).

In the alloys, two types of crack-tip responses are observed; one with the nucleation of a basal $\langle\mathbf{a}\rangle$ dislocation followed by twinning (case I), and the other with the nucleation of the twin directly (case II). In case I (Fig. 11b,e,h), the first $\langle\mathbf{a}\rangle$ dislocation is nucleated at a critical SIF $K_{\mathrm{IIe,Sim}} \approx 0.110$ MPa$\sqrt{\mathrm{m}}$, similar to that in pure Mg. With increasing the applied loads, a $\{11\bar{2}1\}\langle\bar{1}\bar{1}26\rangle$ twin is subsequently nucleated at $K_{\mathrm{II}} \approx 0.135$ MPa$\sqrt{\mathrm{m}}$, 10% lower than that in pure Mg. With further increasing the load to $K_{\mathrm{II}} = 0.160$ MPa$\sqrt{\mathrm{m}}$, the twin grows to 9.9 nm, which is nearly 2 times that in pure Mg. In contrast, a twin is directly nucleated at $K_{\mathrm{IIe,Sim}} \approx 0.110$ MPa$\sqrt{\mathrm{m}}$ in case II (Fig. 11f). The nucleation occurs at local favourable sites and the twin nucleus varies along the crack front (Fig. 12g–i). The nucleated twin grows rapidly in the crack front and twin thickness directions, and reaches a length of $\sim$14 nm approaching the fixed-displacement boundary imposed in the simulation (Fig. 11i).

Fig. 13 reveals the twin growth mechanism. Here, growth takes place through two separate processes: (i) lengthening at the advancing twin tip and (ii) thickening at the TBs. The former is carried out by localized shear/slip to overcome γ_{us} or γ_{utw} manifest in the respective γ_{rc}-lines (Fig. 7b), while the latter is achieved by the nucleation and glide of twinning disconnections. Since the three cases shown in Fig. 13

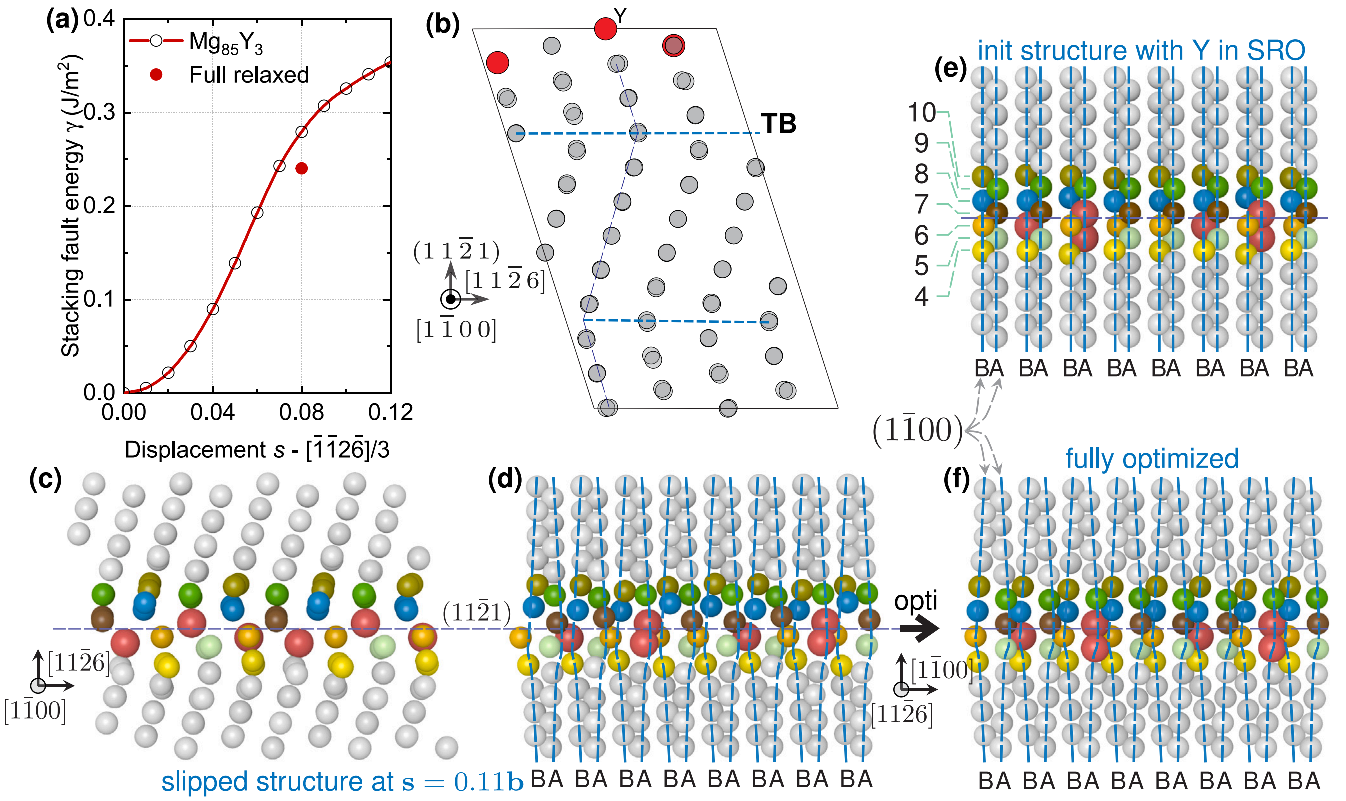

Fig. 10. The $\{11\bar{2}1\}\langle\bar{1}\bar{1}26\rangle$ GSFE γ_{rc}-line and slipped structure in $Mg_{85}Y_3$ with Y solutes in SRO calculated in DFT. (a) The γ_{rc}-line in $Mg_{85}Y_3$. The red solid dot is the energy of the fully relaxed twinned structure in (b). (b) The twin structure obtained from constraint-free optimization of the slipped structure at $\mathbf{s} \approx 0.11\mathbf{b}$. (c–d) The slipped structure at $\mathbf{s} = 0.11\mathbf{b}$ before constraint-free optimization. Substantial shuffling reverses the asymmetry of the $(1\bar{1}00)$ planes. (e) The optimized structure with Y at SRO without slip. No atom shuffling is visible before slip. (f) The fully optimized twinned structure viewed in the $[11\bar{2}6]$ direction (the same structure as that in (b) but showing only one twin boundary and the reversing of the AB layer). In (c–f), the Y atoms are coloured red, and the rest are coloured based on their $\{11\bar{2}1\}$ atom layers numbers from the slip plane. (For interpretation of the references to colour in this figure legend, the reader is referred to the web version of this article.)

are at the same load, the advancement of the twin tip is clearly more difficult in pure Mg than in the Mg–3at.%Y alloy. This is not surprising as no metastable SF exists on the γ_{rc}-line of pure Mg and the actual barrier, as suggested in the multi-layer GPFE profile (Fig. 6), is much larger than γ_{utw} in the alloy.

Twin thickening can proceed if twinning disconnections can nucleate from the free surface at the crack tip. However, this process will be kinematically limited when the twin thickness H grows above the blunted crack-tip height t (e.g., six $\{11\bar{2}1\}$ atom-layers or less in Fig. 3b). Subsequent growth requires nucleation of twinning disconnection dipoles or loops on the flat TBs. In HCP structures, such heterogeneous nucleation on TBs generally has low barriers due to the small twinning Burgers vectors ($|\mathbf{b}_t| = 0.94$ Å, and see Ref. [65]), which is distinctly different from that in FCC structures [25,26,55,58]. In case II of Mg–3at.%Y, twinning disconnection dipoles can be nucleated continuously on the earlier flat TBs and H reaches more than $2t$, resulting in the lenticular twin shape observed in a broad range of experiments in Mg–RE alloys [15–17]. In contrast, deformation twinning typically has a nanoscale, rectangular shape in FCC structures [66] where twinning disconnections are difficult to nucleate on the flat TBs, leaving stress concentrations such as GBs [27] or crack-tips [25,26,58] as the primary twin nucleation sites.

Furthermore, nucleation of twinning disconnection dipoles will also be influenced by other nearby disconnections nucleated earlier (via their elastic interactions), which in turn is affected by how far the twin tip can propagate. As a result, the nucleated twin only grows to a height H of 7 atom layers in pure Mg, while the two cases in Mg–3at.% Y reach 11 and 14 atom layers at the same load $K_{II} = 0.160$ MPa$\sqrt{\text{m}}$. In case II Mg–3at.%Y, the twin tip advancement is constrained as it approaches the fixed boundary in the current simulation (Fig. 11i, similar to constraints at grain boundaries which break lattice continuity). The twin length would presumably be larger in bulk grains where the boundary effects are remote and twinning disconnection dipoles can be nucleated continuously on the earlier flat TBs. Overall, the prevalence of the $\{11\bar{2}1\}\langle\bar{1}\bar{1}26\rangle$ deformation twinning is limited by nucleation and advancement of the twin tip, while twin thickening is generally not the limiting factor in Mg or MgY alloys with dilute Y concentrations.

Fig. 14 shows the measured twin length as a function of the applied load for all the sampled cases. In Mg–1.5at.%Y and Mg–3at.%Y, all random configurations show twin nucleation at similar or lower K_{II} compared to that in pure Mg. The critical loads $K_{IIe,Sim}$ where the twin length becomes appreciable (≥2 nm) is 0.135 MPa$\sqrt{\text{m}}$ and 0.110 MPa$\sqrt{\text{m}}$ in case I and II, which are close to $K_{IIe,Rice} = 0.125$ MPa $\sqrt{\text{m}}$ based on the Rice criterion with $\gamma_{utw} = 0.3$ J/m^2 from Fig. 7b and elastic properties of the interatomic potential (Eq. (2)). The corresponding critical load is $K_{IIe,Sim} = 0.150$ MPa$\sqrt{\text{m}}$ in pure Mg, which is ∼36% higher than that of the most favourable configuration in case II of Mg–3at.%Y. Comparing the two Y solute concentrations, the cases in the higher Y concentration alloy generally have lower critical loads and higher growth rates in both case I and II, which is also consistent with MgGd experiments where the relative frequency of the $\{11\bar{2}1\}$ twin increases with the concentration of Gd and the $\{11\bar{2}1\}$ twin becomes more prevalent than the competing $\{10\bar{1}2\}$ twin at 2.44 at.%Gd [20]. In contrast, nearly all cases (except one in case II) in Mg–3at.%Al have almost the same critical load and growth rate as that in pure Mg, suggesting the ineffectiveness of Al solutes on the activation of the $\{11\bar{2}1\}$ twin and consistent with broad experimental observations in MgAl alloys.

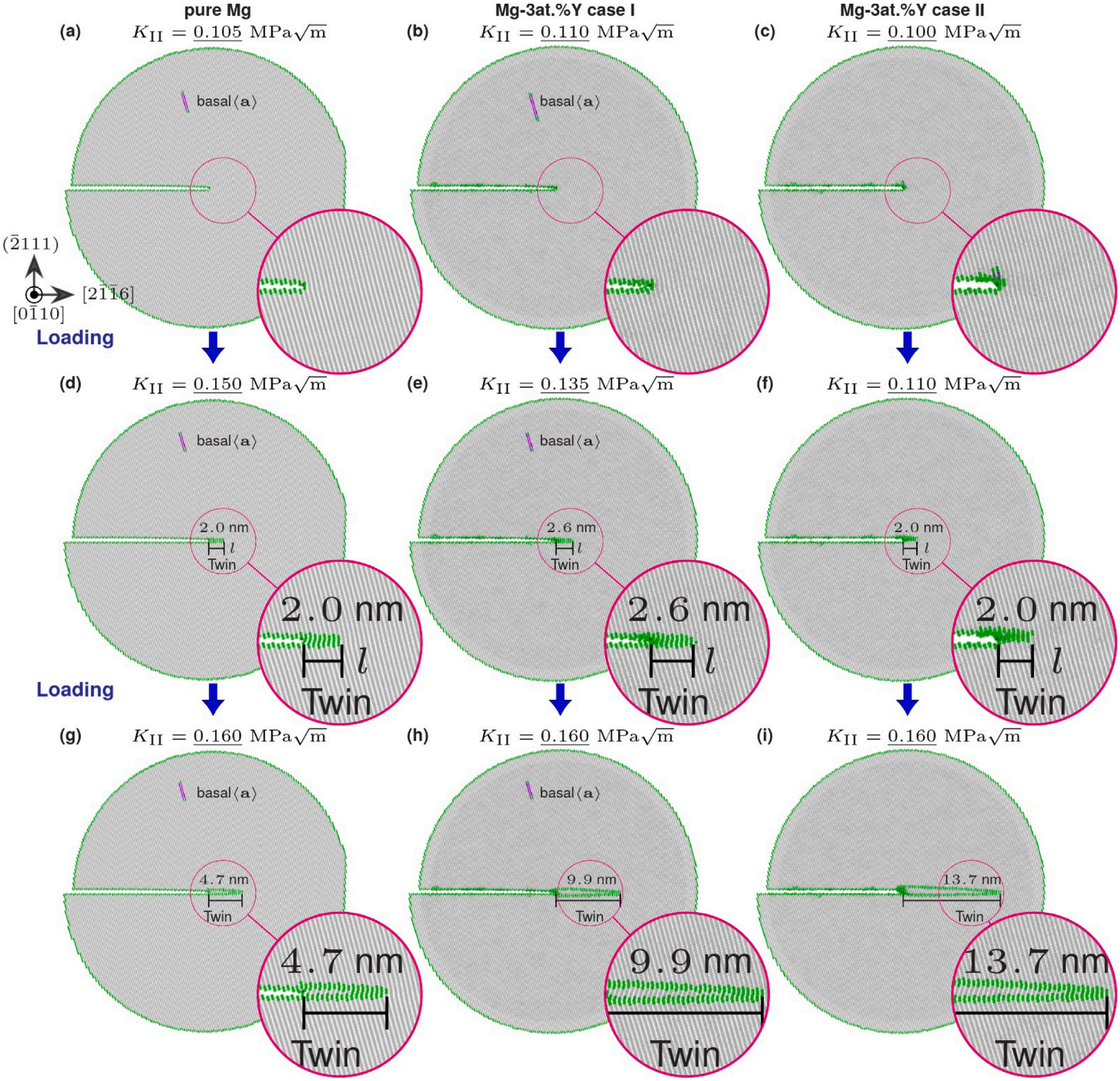

Fig. 11. Crack tip behaviour under mode-II loadings in atomistic simulations using the XMEAM potential for the MgY binary system. (a, d, g) Pure Mg. (b, e, h) Case I in Mg–3at.%Y. (c, f, i) Case II in Mg–3at.%Y. A basal ⟨**a**⟩ dislocation is emitted first, followed by the nucleation and growth of the $\{11\bar{2}1\}\langle\bar{1}\bar{1}26\rangle$ twin in Pure Mg and case I of Mg–3at.%Y, while the $\{11\bar{2}1\}\langle\bar{1}\bar{1}26\rangle$ twin is nucleated directly in case II of Mg–3at.%Y. The top row shows the crack-tip configurations just after the emission of the basal ⟨**a**⟩ or just before the twin embryo nucleation; the middle row shows the tip configurations when the twin embryo is formed; the bottom row shows the respective systems at the same load of $K_{\mathrm{II}} = 0.160$ MPa$\sqrt{\mathrm{m}}$. Atoms are coloured based on their atomic environment identified using the adaptive common neighbour analysis (aCNA [64]): hcp-grey, fcc-purple and others-green. (For interpretation of the references to colour in this figure legend, the reader is referred to the web version of this article.)

Furthermore, the nucleation and growth show minor variations within the case I and II random configurations, even though γ_{utw} depends on local solute fluctuations in the alloy. Given the small variations, we can use the measured critical SIF $K_{\mathrm{IIe,Sim}}$ to estimate the effective γ_{utw} for activating twinning using the Rice criterion, neglecting the details in nucleation path. For example, using $K_{\mathrm{IIe,Sim}} = 0.110, 0.135$ from the simulations, the effective γ_{utw} based on Eq. (2) are in the range of $\gamma_{\mathrm{utw}} \in \{0.23, 0.35\}$ J/m^2, which is comparable to $\gamma_{\mathrm{utw}} = 0.255$ J/m^2 for nucleating the competing $\{10\bar{1}2\}\langle10\bar{1}1\rangle$ extension twin in pure Mg. Similarly, the effective γ_{utw} is 0.4 J/m^2 for the $\{11\bar{2}1\}\langle\bar{1}\bar{1}26\rangle$ twin in pure Mg. In addition, all twins grow to longer lengths at the same load in the alloy when compared to that in pure Mg. Once nucleated, all the cases have similar twin length growth rate $\partial l/\partial K_{\mathrm{II}}$. Nonetheless, the absolute K_{II} is always ~50% higher in pure Mg than that in case II of Mg–3at.%Y. Clearly, in the absence of a metastable SF in pure Mg (Fig. 6), higher K_{II} loads are required to drive the twin tip advancement overcoming the higher barrier, even after successful nucleation at the crack-tip.

While the above sampling using 8 random configurations is not exhaustive, it provides a validation of the proposed mechanism based on the DFT-calculated γ_{rc}, i.e., the slip driven, Y solute-enhanced shuffle displacement induces a metastable SF in the $[\bar{1}\bar{1}2\bar{6}]$ twinning direction

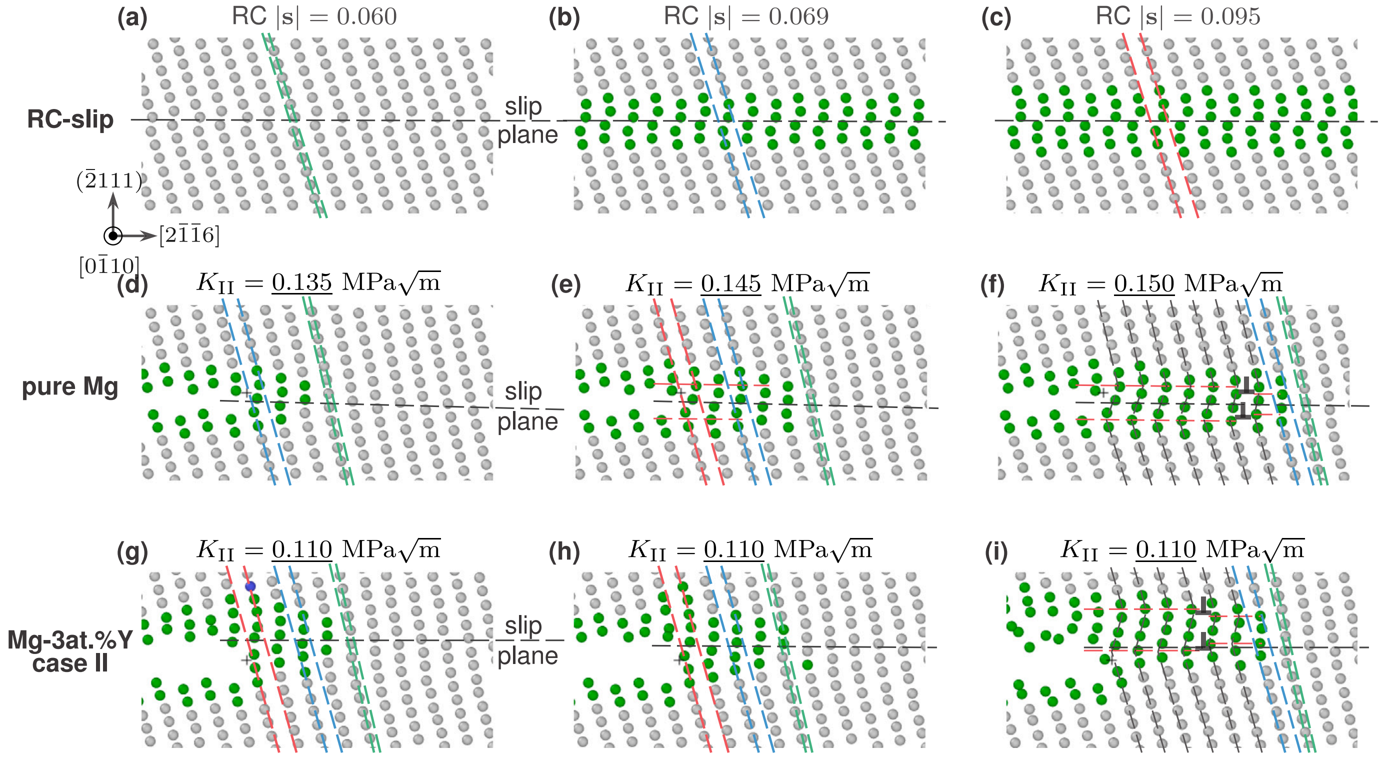

Fig. 12. Comparison of configurations on the reduced-constraint (RC) path and at the crack-tips. (a–c) Configurations at various slip steps on the RC path. All structures are unstable and revert back to the perfect HCP lattice upon constraint-free structure optimization. (d–f) Configurations at the crack-tip at various K_{II} loadings in pure Mg. A twin embryo of 4 atom-layers are formed in (f) at $K_{II} = 0.150$ MPa$\sqrt{\text{m}}$. (g–i) Configurations at the crack-tip at $K_{II} = 0.110$ MPa$\sqrt{\text{m}}$ in case II of Mg–3at.%Y. The three configurations are taken at different slices along the crack front. A twin embryo of 5 atom-layers are formed in (i). See Fig. 11 caption for interpretations of atom colours.

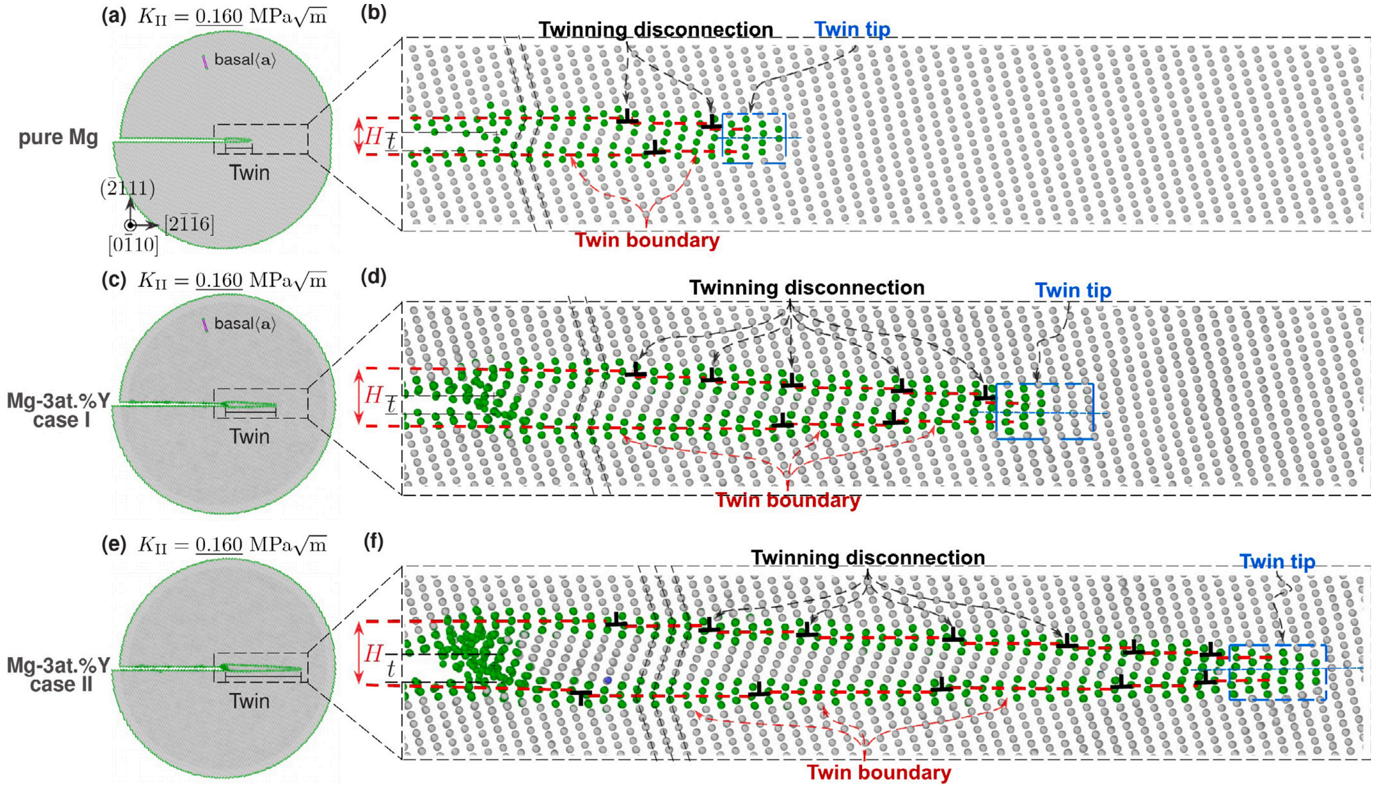

Fig. 13. Twin growth at the crack-tip by (i) lengthening at the advancing tip and (ii) thickening via the nucleation and glide of twinning disconnections at the twin boundaries. (a, b) Pure Mg. (c, d) Case I in Mg–3at.%Y. (e, f) Case II in Mg–3at.%Y. In all the cases, the crack models are loaded to the same $K_{II} = 0.160$ MPa$\sqrt{\text{m}}$. When the twin thickness (number of $\{11\bar{2}1\}$ atom layers) grows larger than the initial crack bluntness, further twin thickening is realized by homogeneous nucleation of disconnection dipoles near the crack tip, resulting in a twin of lenticular shape and in agreement with a previous model [65]. See Fig. 11 caption for interpretations of atom colours.

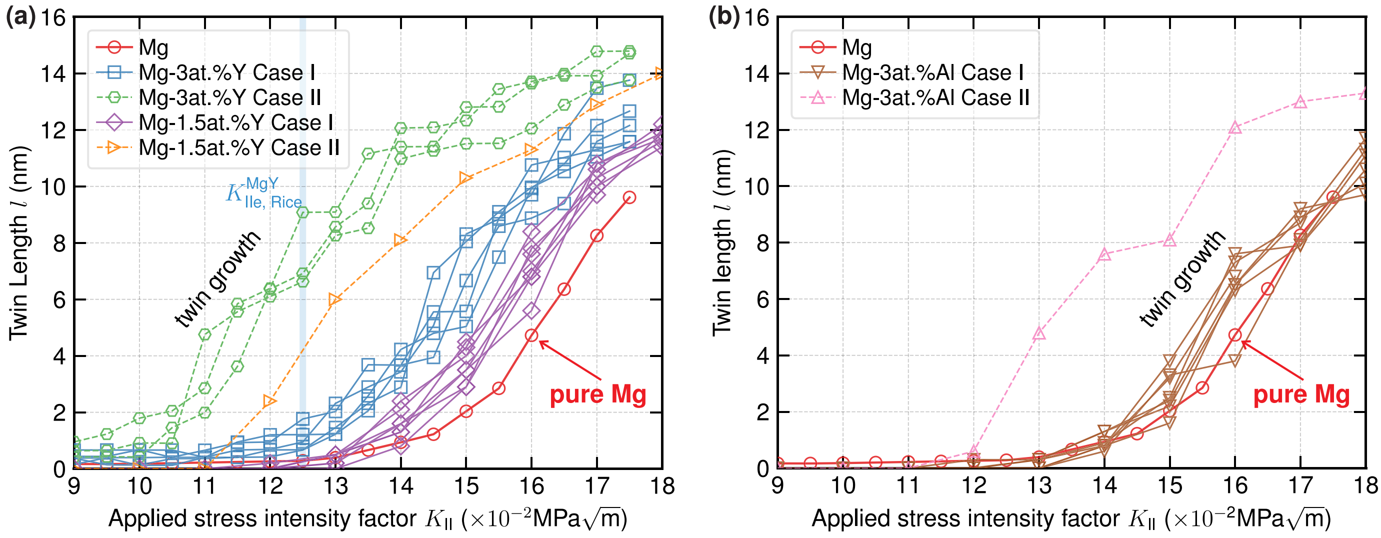

Fig. 14. The twin length as a function of applied stress intensity factor K_{II} load. (a) Mg, Mg–1.5at.%Y and Mg–3at.%Y. (b) Mg and Mg–3at.%Al. The length of the twin l is taken as the horizontal distance between the crack tip and the twin tip. The twin tip is defined as the boundary separating the HCP and non-HCP atoms identified by aCNA [64] (Fig. 13). The solid and dashed lines denote two typical responses in Mg alloys: case I emission of a basal ⟨**a**⟩ dislocation followed by twin nucleation, and case II direct twin nucleation, respectively. The vertical blue line marks the critical load $K_{IIe,Rice}$ predicted by the Rice criterion for Mg–3at.%Y (Eq. (2)).

on the $(11\bar{2}1)$ twinning plane, which in turn enables direct formation of the $\{11\bar{2}1\}\langle\bar{1}\bar{1}26\rangle$ twin nucleus, reduces the barrier to the advancement of the twin-tip, and enhances twin growth. If more samplings were conducted, the critical SIFs will be a distribution around the values shown in Fig. 14. In experiments of bulk alloy samples, more favourable nucleation sites should exist with even lower critical SIF K_{IIe}. Deformation twinnings, such as the case II shown here, will thus be activated first, which in turn relieves local shear stress concentrations and prevents or delays activations of other deformation mechanisms such as basal ⟨**a**⟩ slips or the competing $\{10\bar{1}2\}\langle10\bar{1}1\rangle$ extension twins.

Finally, we examine the stability of the nucleated twins. The applied K_{II} loads are reversed to the respective threshold values corresponding to the formation of the twin nucleus. Fig. 15 shows the comparison of twin structures along the loading and unloading paths. For pure Mg (Fig. 15a,d,g), the twin length l and heigh H first increase from 2.0 nm to 4.7 nm and from 4 atom-layers to 7 atom-layers with a load increment ΔK_{II} = 0.01 MPa$\sqrt{\text{m}}$, and then reduces to 2.3 nm upon reversing ΔK_{II}. The twin thus nearly completely reverts to its initial structure with only the earlier twin nucleus remaining (Figs. 11d and 12f), suggesting that the twinning disconnections have a relatively low migration barrier/lattice friction. This is consistent with (i) their small Burger vectors ($|\mathbf{b}_t|$ = 0.94 Å) and (ii) the corresponding γ_{rc}-line (Fig. 4b) where no metastable SF is present and the localized shear at the twin tip is unstable. In the alloys, the twins exhibit similar growths as that in pure Mg with increasing load ΔK_{II}, although the absolute K_{II} values are lower. Upon reducing the same load ΔK_{II}, the twin length l shrinks by 0.8 nm and 1.9 nm in case I and II, but the remaining twin length is nearly two times that in pure Mg. The larger remaining twin length in the alloy may arise from at least two factors: the increased friction of the twinning disconnection due to Y solutes and the metastable twin nucleus manifest on the γ_{rc} line. Overall, the load–unload cycle and the twin growth shown in Fig. 13 together suggest that the Y solutes facilitate twin nucleation and twin tip advancement, while Y solutes increase the lattice friction of the twinning disconnections but such increase does not retard twin growth (Fig. 14).

4. Discussion

The above simulations give a qualitative trend of the effects of Y solutes rather than a quantitative prediction of the exact solute concentration and critical SIF for the twin nucleation. These simulations validate the DFT-based γ_{rc} analysis and reveal the physical mechanism of Y-enhanced $\{11\bar{2}1\}\langle\bar{1}\bar{1}26\rangle$ twinnability in MgY alloys. The new mechanism is distinctly different from previous models. For example, the prevalence of $\{11\bar{2}1\}$ twins was phenomenologically attributed to the reduction of TB energy by Gd [20]. However, in solution-treated Mg–RE alloys, solutes are distributed randomly or with some SRO. Operation of the $\{11\bar{2}1\}$ twinning requires 2 steps: nucleation and growth. Nucleation occurs at local favourable positions as shown in $Mg_{70}Y_2$ and $Mg_{85}Y_3$, while growth is carried out by TB disconnection glide and twin tip advancement, which sample through a random or SRO solute environment. If Y solutes substantially reduce the $\{11\bar{2}1\}$ TB energy (negligible at 3at.% in random distribution), they would exert a strong solute pining effects on TB migration and thus slow twin growth [67]. The effects of Y/Gd on TB energy thus do not directly promote the activation or growth of the $\{11\bar{2}1\}$ twin. Furthermore, the TBs here are always at several atom layers away from the Y solutes, since the twin nucleus is first formed by Y-enhanced shuffling and the TBs migrate in both directions away from the Y-sites (Fig. 7c,d). The final TB energy with or without Y again is not directly relevant to the twin nucleation.

Separately, the activation of the $\{11\bar{2}1\}$ twin was also attributed to the change of c/a induced by solutes [17], since Y reduces c/a towards that in Re, Zr and Ti [17,68,69]. However, the reduction is rather small (0.01 at 5wt.%Y [68]) and insensitive to ageing treatment. Furthermore, Co has nearly the same c/a as Mg (∼1.623 vs. ∼1.624), and exhibits $\{11\bar{2}1\}$ twins intrinsically [14], while Be has a much lower c/a (∼1.568) and $\{11\bar{2}1\}$ twinning is not reported. Therefore, change of c/a is unlikely responsible for the activation of the $\{11\bar{2}1\}$ twins in Mg–RE alloys either. Furthermore, the $\{11\bar{2}1\}$ twin activation may be ascribed to hardening of other deformation modes by RE solutes since they increase the yield and flow stresses [15–17]. However, if stress were the primary limiting factor, the $\{11\bar{2}1\}$ twins would be activated in pure Mg or any other alloys capable of reaching a flow stress between ∼200 MPa and ∼300 MPa where the $\{11\bar{2}1\}$ twins are observed in Mg–RE [16,17]. Such stresses are not uncommon in Mg alloys, e.g., Mg–Al [70], Mg–Zn [71,72], Mg–Al–Ca [73,74], AZ91 [75], WE43 [76]. However, the $\{11\bar{2}1\}$ twins are not reported in such alloys (e.g., Mg–3Al–1Zn–0.4Mn [77]). In addition, the $\{11\bar{2}1\}$ twin is reported in solution-treated (ST) WE54, but not seen after precipitation treatment which presumably increases the CRSS of all dislocations to levels higher than that in solid solution state and favours the $\{11\bar{2}1\}$

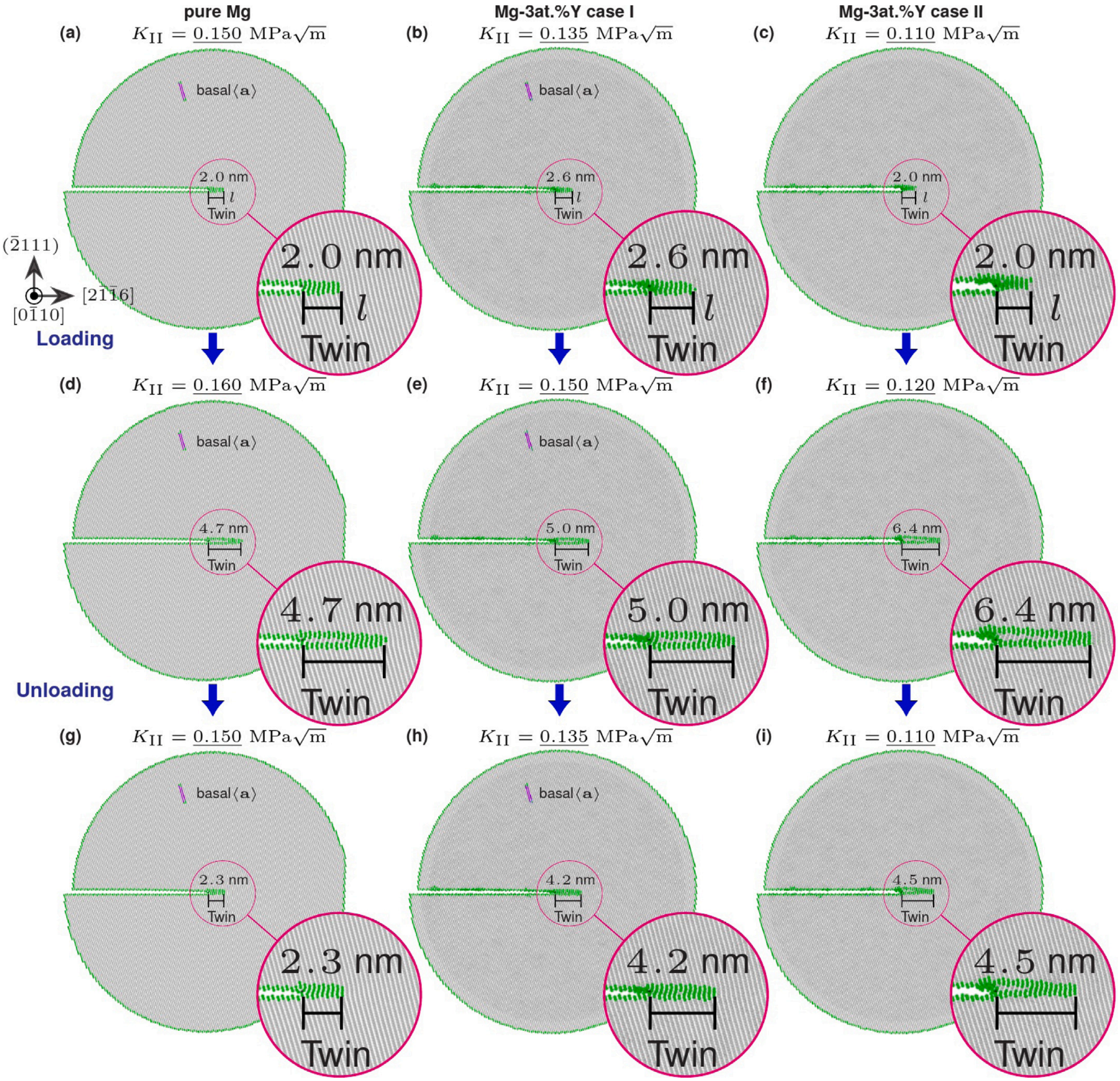

Fig. 15. Crack-tip responses during incremental mode-II loading and unloading. (a, d, g) Pure Mg. (b, e, h) Case I in Mg–3at.%Y. (c, f, i) Case II in Mg–3at.%Y. The top row shows the crack-tip configurations when the twin embryo is just formed during load increments; the middle row shows crack-tip configurations when the twin grows under further increasing loads; the bottom row shows the crack-tip configurations after unloading to the same SIF as that in the top row. See Fig. 11 caption for interpretations of atom colours.

twin activation [18]. Therefore, extant experiments do not support the stress-limited/CRSS hypothesis.

In the current study, although the $\{11\bar{2}1\}\langle\bar{1}\bar{1}26\rangle$ twin is activated in pure Mg, MgY and MgAl alloys, the twin nucleation and growth clearly become easier with increasing Y concentration as in experiments. Additional simulations are performed with higher Y concentrations (5at.% and 10 at.% above its solubility) and show similar or further increased Y-enhanced $\{11\bar{2}1\}\langle\bar{1}\bar{1}26\rangle$ twinnability in Mg. In the alloys, the key difference between case I and II lies in the nucleation of the first basal ⟨**a**⟩ dislocation, which changes the crack-tip geometry, reduces the crack height t to only 2 atom-layers and leads to early onset of disconnection dipole nucleations. In sharp cracks loaded in mode II or a mix of mode I and II, twin nucleation may still be possible through direct nucleation of the twinning disconnection dipoles at crack tips. Such mechanisms are not considered to be viable in FCC structures, but is highly likely in Mg and other HCP metals. Future works may thus study the crack-tip responses with different loadings, tip geometries, crack front lengths, solute distributions, sample radii, as well as thermal activations. With the present XMEAM interatomic potentials for MgY and MgAl [61], the competition among all dislocation and twinning modes, as well as their dependence on solutes, can also be studied systematically. Direct MD simulations can also be performed using polycrystalline samples to reveal twin nucleation and growth at GBs. In addition, the exact twin nucleation path in pure Mg is not explicitly determined, since the multilayer slip path only provides an upper bound and the stable twin nucleus has not been revealed (Fig. 6). Instead, an effective $\gamma_{\rm utw}$ is measured directly in the mode-II loaded crack simulation. This twin nucleus is only stabilized under the large shear stress of the crack-tip, similar to that in W [30,36,78]. Further study is being carried out to determine stress effects and the minimum stable twin thickness in pure Mg.

Separately, the RC method [6,30,35] is general. It can be extended to calculate $\gamma_{\rm rc}$-lines on other slip planes and determine the relevant transition paths and energetics for both dislocation and twin nucleations. For example, preliminary DFT calculations have been carried out for the $\langle 1 0 \bar{1} 1\rangle$ twin on the $\{1 0 \bar{1} 2\}$ plane in pure Mg. A meta-stable point (not present in the classical γ-line) is revealed at slip $\mathbf{s} \approx \mathbf{b}_{\rm b}$ in the $\langle 1 0 \bar{1} 1\rangle$ twinning direction on the $\gamma_{\rm rc}$-lines using DFT and the XMEAM potential for Mg. The corresponding meta-stable structure spontaneously transforms into a twin structure. The barrier for this twin nucleation is similar to or slightly lower than that for $\langle \mathbf{c}+\mathbf{a}\rangle$ dislocations on the pyramidal I and II planes, consistent with experimental observations that the $\langle 1 0 \bar{1} 1\rangle\{1 0 \bar{1} 2\}$ twin is prevalent in deformation of pure Mg. Following this approach, the barriers for different dislocation and twin nucleations can be systematically determined across all HCP systems, which will eventually reveal the activation and preference among competing deformation mechanisms. These details, particularly the general trend across all HCP structures, will be reported in future works.

In summary, we reveal the physical origin for the activation of the $\{1 1 \bar{2} 1\}\langle \bar{1} \bar{1} 2 6\rangle$ deformation twin in Mg upon Y solute additions. Twinning can be activated by (i) localized slip which provides the shear displacements in the twinning direction on the twinning plane and (ii) Y-solutes enhanced shuffle displacements in the perpendicular direction. The combined shear and shuffle lead to spontaneous formation of the twin nucleus at an energy barrier comparable to or lower than that for other deformation mechanisms. Since the mechanism is based on crystal geometry of the twinning plane, is seen in both random and SRO solute environment, and correctly distinguishes the effect of different solutes (Y and Al), it is expected to be general in other Mg–RE solid solution alloys. The activation of new twinning mode may provide an alternative mechanism to increase plasticity and toughness in the intrinsically brittle Mg; it may help blunt crack-tips and thus arrest their fast propagation. Direct atomistic simulations will be useful to study this new phenomenon fully across a wide range of Mg alloys when accurate interatomic potentials (such as the current XMEAM for MgY) are available for such Mg-based alloy systems. Furthermore, the current work provides a general computational approach to quantitatively investigate twinning paths, associated energy barriers, as well as alloying effects across the HCP family.

CRediT authorship contribution statement

Jianwei Xiao: Writing – original draft, Methodology, Investigation, Formal analysis, Conceptualization. **Junjie Gao:** Methodology, Investigation, Formal analysis. **Songwei Li:** Writing – original draft, Methodology, Investigation, Formal analysis. **Rui Wang:** Methodology, Investigation, Formal analysis. **Chuang Deng:** Resources, Investigation, Formal analysis. **Yuntian Zhu:** Supervision, Project administration, Funding acquisition, Formal analysis. **Zhaoxuan Wu:** Writing – review & editing, Writing – original draft, Supervision, Project administration, Methodology, Investigation, Funding acquisition, Formal analysis, Conceptualization.

Declaration of competing interest

The authors declare that they have no known competing financial interests or personal relationships that could have appeared to influence the work reported in this paper.

Acknowledgements

This work is supported by the National Key R&D Program of China (2021YFA1200202), the Research Grants Council, Hong Kong SAR through the Early Career Scheme and General Research Fund (21205019, 11217522, 11216423), CityU Donations for Research Projects (9229077), Strategic Research Grant, China (CityU 11219721), and the National Natural Science Foundation of China (51931003). J.G., R.W., Z.W. and Y.Z. gratefully acknowledge the sponsorship from the Hong Kong Institute for Advanced Study, City University of Hong Kong, under the project number 9360157. Computational resources are provided by Compute Canada and the computational facilities, CityU Burgundy, managed and provided by the Computing Services Centre at City University of Hong Kong (https://www.cityu.edu.hk/).

References

[1] M.H. Yoo, Slip, twinning, and fracture in hexagonal close-packed metals, Metall. Trans. A 12 (1981) 409–418, http://dx.doi.org/10.1007/BF02648537.

[2] T.B. Britton, F.P.E. Dunne, A.J. Wilkinson, On the mechanistic basis of deformation at the microscale in hexagonal close-packed metals, Proc. R. Soc. A 471 (2178) (2015) 20140881, http://dx.doi.org/10.1098/rspa.2014.0881.

[3] Z. Wu, W.A. Curtin, The origins of high hardening and low ductility in magnesium, Nature 526 (7571) (2015) 62–67, http://dx.doi.org/10.1038/nature15364.

[4] T. Wen, A. Liu, R. Wang, L. Zhang, J. Han, H. Wang, D.J. Srolovitz, Z. Wu, Modelling of dislocations, twins and crack-tips in HCP and BCC Ti, Int. J. Plast. 166 (2023) 103644, http://dx.doi.org/10.1016/j.ijplas.2023.103644.

[5] Z. Wu, W.A. Curtin, Brittle and ductile crack-tip behavior in magnesium, Acta Mater. 88 (2015) 1–12, http://dx.doi.org/10.1016/j.actamat.2015.01.023.

[6] B. Yin, Z. Wu, W.A. Curtin, Comprehensive first-principles study of stable stacking faults in hcp metals, Acta Mater. 123 (2017) 223–234, http://dx.doi.org/10.1016/j.actamat.2016.10.042.

[7] Z. Wu, B. Yin, W.A. Curtin, Energetics of dislocation transformations in hcp metals, Acta Mater. 119 (2016) 203–217, http://dx.doi.org/10.1016/j.actamat.2016.08.002.

[8] J.W. Christian, S. Mahajan, Deformation twinning, Prog. Mater. Sci. 39 (1–2) (1995) 1–157, http://dx.doi.org/10.1016/0079-6425(94)00007-7.

[9] A. Jain, O. Duygulu, D. Brown, C. Tomé, S. Agnew, Grain size effects on the tensile properties and deformation mechanisms of a magnesium alloy, AZ31B, sheet, Mater. Sci. Eng. A 486 (1–2) (2008) 545–555, http://dx.doi.org/10.1016/j.msea.2007.09.069.

[10] J.C. Williams, R.G. Baggerly, N.E. Paton, Deformation behavior of HCP Ti–Al alloy single crystals, Metall. Mater. Trans. A 33 (3) (2002) 837–850, http://dx.doi.org/10.1007/s11661-002-0153-y.

[11] S. Jin, K. Marthinsen, Y. Li, Formation of $\{11\bar{2}1\}$ twin boundaries in titanium by kinking mechanism through accumulative dislocation slip, Acta Mater. 120 (2016) 403–414, http://dx.doi.org/10.1016/j.actamat.2016.08.042.

[12] P.-A. Juan, C. Pradalier, S. Berbenni, R. McCabe, C. Tomé, L. Capolungo, A statistical analysis of the influence of microstructure and twin–twin junctions on twin nucleation and twin growth in Zr, Acta Mater. 95 (2015) 399–410, http://dx.doi.org/10.1016/j.actamat.2015.05.022.

[13] M. de Jong, J. Kacher, M.H.F. Sluiter, L. Qi, D.L. Olmsted, A. van de Walle, J.W. Morris, A.M. Minor, M. Asta, Electronic origins of anomalous twin boundary energies in hexagonal close packed transition metals, Phys. Rev. Lett. 115 (6) (2015) 065501, http://dx.doi.org/10.1103/physrevlett.115.065501.

[14] Y. Zhu, X. Zhang, H. Ni, F. Xu, J. Tu, C. Lou, Formation of $\{11\bar{2}1\}$ twins in polycrystalline cobalt during dynamic plastic deformation, Mater. Sci. Eng. A 548 (2012) 1–5, http://dx.doi.org/10.1016/j.msea.2012.03.017.

[15] K.H. Eckelmeyer, R.W. Hertzberg, Deformation in wrought Mg–9Wt Pct Y, Metall. Trans. 1 (12) (1970) 3411–3414, http://dx.doi.org/10.1007/bf03037872.

[16] N. Stanford, R.K.W. Marceau, M.R. Barnett, The effect of high yttrium solute concentration on the twinning behaviour of magnesium alloys, Acta Mater. 82 (2015) 447–456, http://dx.doi.org/10.1016/j.actamat.2014.09.022.

[17] N. Ansari, S.Y. Lee, S.S. Singh, J. Jain, Influence of yttrium-induced twinning on the recrystallization behavior of magnesium alloys, J. Mater. Sci. 56 (32) (2021) 18258–18271, http://dx.doi.org/10.1007/s10853-021-06418-8.

[18] N. Stanford, Observation of $\{11\bar{2}1\}$ twinning in a Mg-based alloy, Phil. Mag. Lett. 88 (5) (2008) 379–386, http://dx.doi.org/10.1080/09500830802070793.

[19] Y. Zhu, S. Xu, J. Nie, $\{10\bar{1}1\}$ twin boundary structures in a Mg–Gd alloy, Acta Mater. 143 (2018) 1–12, http://dx.doi.org/10.1016/j.actamat.2017.09.067.

[20] C. He, Z. Li, D. Kong, X. Zhao, H. Chen, J.-F. Nie, Origin of profuse $\{11\bar{2}1\}$ deformation twins in Mg–Gd alloys, Scr. Mater. 191 (2021) 62–66, http://dx.doi.org/10.1016/j.scriptamat.2020.08.041.

[21] H. Zhou, G.M. Cheng, X.L. Ma, W.Z. Xu, S.N. Mathaudhu, Q.D. Wang, Y.T. Zhu, Effect of Ag on interfacial segregation in Mg–Gd–Y–(Ag)–Zr alloy, Acta Mater. 95 (2015) 20–29, http://dx.doi.org/10.1016/j.actamat.2015.05.020.

[22] J. Li, Z. Dong, X. Yi, D. Wu, R. Chen, Twin evolution in cast Mg–Gd–Y alloys and its dependence on aging heat treatment, J. Magn. Alloys 11 (7) (2023) 2285–2298, http://dx.doi.org/10.1016/j.jma.2021.09.023.

[23] H. Fan, J.A. El-Awady, Molecular dynamics simulations of orientation effects during tension, compression, and bending deformations of magnesium nanocrystals, J. Appl. Mech. 82 (10) (2015) 101006, http://dx.doi.org/10.1115/1.4030930.

[24] V. Vítek, Intrinsic stacking faults in body-centred cubic crystals, Phil. Mag. 18 (154) (1968) 773–786, http://dx.doi.org/10.1080/14786436808227500.

[25] E.B. Tadmor, S. Hai, A Peierls criterion for the onset of deformation twinning at a crack tip, J. Mech. Phys. Solids 51 (5) (2003) 765–793, http://dx.doi.org/10.1016/S0022-5096(03)00005-X.

[26] E.B. Tadmor, N. Bernstein, A first-principles measure for the twinnability of FCC metals, J. Mech. Phys. Solids 52 (11) (2004) 2507–2519, http://dx.doi.org/10.1016/j.jmps.2004.05.002.

[27] R.J. Asaro, S. Suresh, Mechanistic models for the activation volume and rate sensitivity in metals with nanocrystalline grains and nano-scale twins, Acta Mater. 53 (12) (2005) 3369–3382, http://dx.doi.org/10.1016/j.actamat.2005.03.047.

[28] L. Zhu, Z. Wu, Effects of short range ordering on the generalized stacking fault energy and deformation mechanisms in FCC multiprincipal element alloys, Acta Mater. 259 (2023) 119230, http://dx.doi.org/10.1016/j.actamat.2023.119230.

[29] T. Wen, R. Wang, L. Zhu, L. Zhang, H. Wang, D.J. Srolovitz, Z. Wu, Specialising neural network potentials for accurate properties and application to the mechanical response of titanium, NPJ Comput. Mater. 7 (1) (2021) 206–211, http://dx.doi.org/10.1038/s41524-021-00661-y.

[30] J. Xiao, L. Zhu, R. Wang, C. Deng, Z. Wu, Y. Zhu, Unveiling deformation twin nucleation and growth mechanisms in BCC transition metals and alloys, Mater. Today 65 (2023) 90–99, http://dx.doi.org/10.1016/j.mattod.2023.03.028.

[31] V. Vítek, Multilayer stacking faults and twins on $\{211\}$ planes in B.C.C. metals, Scr. Metall. 4 (9) (1970) 725–732, http://dx.doi.org/10.1016/0036-9748(70)90214-0.

[32] S. Ogata, J. Li, S. Yip, Energy landscape of deformation twinning in bcc and fcc metals, Phys. Rev. B 71 (22) (2005) 224102–224111, http://dx.doi.org/10.1103/PhysRevB.71.224102.

[33] R.C. Pond, J.P. Hirth, A. Serra, D.J. Bacon, Atomic displacements accompanying deformation twinning: shears and shuffles, Mater. Res. Lett. 4 (4) (2016) 185–190, http://dx.doi.org/10.1080/21663831.2016.1165298.

[34] A.H. Faisal, C.R. Weinberger, Modeling twin boundary structures in body centered cubic transition metals, Comput. Mater. Sci. 197 (2021) http://dx.doi.org/10.1016/j.commatsci.2021.110649, 110649–13.

[35] J.R. Morris, J. Scharff, K.M. Ho, D.E. Turner, Y.Y. Ye, M.H. Yoo, Prediction of a $\{11\bar{2}2\}$ hcp stacking fault using a modified generalized stacking-fault calculation, Phil. Mag. A 76 (5) (1997) 1065–1077, http://dx.doi.org/10.1080/01418619708200015.

[36] J. Xiao, S. Li, X. Ma, J. Gao, C. Deng, Z. Wu, Y. Zhu, Origin of deformation twinning in bcc tungsten and molybdenum, Phys. Rev. Lett. 131 (13) (2023) 136101, http://dx.doi.org/10.1103/physrevlett.131.136101.

[37] J.R. Rice, Dislocation nucleation from a crack tip: An analysis based on the peierls concept, J. Mech. Phys. Solids 40 (2) (1992) 239–271, http://dx.doi.org/10.1016/S0022-5096(05)80012-2.

[38] Q. Zhu, Y. Li, Z. Ding, J. Wang, Y. Liu, H. Zhang, T. Xie, M. Wang, H. Zhu, T. Ying, et al., Unveiling precipitation behavior in Mg–Y based alloys, Mater. Des. 202 (2021) 109570, http://dx.doi.org/10.1016/j.matdes.2021.109570.

[39] R. Ahmad, S. Groh, M. Ghazisaeidi, W.A. Curtin, Modified embedded-atom method interatomic potential for Mg–Y alloys, Modelling Simul. Mater. Sci. Eng. 26 (6) (2018) 065010, http://dx.doi.org/10.1088/1361-651x/aacfd2.

[40] M. Nishijima, K. Yubuta, K. Hiraga, Characterization of β' precipitate phase in Mg-2 at%Y alloy aged to peak hardness condition by high-angle annular detector dark-field scanning transmission electron microscopy (HAADF-STEM), Mater. Trans. 48 (1) (2007) 84–87, http://dx.doi.org/10.2320/matertrans.48.84.

[41] W. Lefebvre, V. Kopp, C. Pareige, Nano-precipitates made of atomic pillars revealed by single atom detection in a Mg–Nd alloy, Appl. Phys. Lett. 100 (14) (2012) 141906, http://dx.doi.org/10.1063/1.3701272.

[42] J.F. Nie, N.C. Wilson, Y.M. Zhu, Z. Xu, Solute clusters and GP zones in binary Mg–RE alloys, Acta Mater. 106 (2016) 260–271, http://dx.doi.org/10.1016/j.actamat.2015.12.047.

[43] D. Egusa, K. Kawaguchi, E. Abe, Direct observations of precursor short-range order clusters of solute atoms in a LPSO-forming Mg–Zn–Gd ternary alloy, Front. Mater. 6 (2019) 266, http://dx.doi.org/10.3389/fmats.2019.00266.

[44] H. Su, G. Tian, C. Zhang, S. Wang, C. Xue, J. Wang, S. Guan, Quantitative evaluation of the short-range order strengthening effect on solid solution and GB strength of Mg–Y alloys by ab initio calculations, J. Mater. Sci. 57 (42) (2022) 19986–20001, http://dx.doi.org/10.1007/s10853-022-07823-3.

[45] J.A. Nieminen, A.P. Sutton, J.B. Pethica, Static junction growth during frictional sliding of metals, Acta Metall. Mater. 40 (10) (1992) 2503–2509, http://dx.doi.org/10.1016/0956-7151(92)90320-E.

[46] A.P. Sutton, R.W. Balluffi, Interfaces in Crystalline Materials, Clarendon Press, 1995.

[47] S. Kibey, J.B. Liu, D.D. Johnson, H. Sehitoglu, Generalized planar fault energies and twinning in Cu–Al alloys, Appl. Phys. Lett. 89 (19) (2006) 191911–191913, http://dx.doi.org/10.1063/1.2387133.

[48] G. Kresse, J. Furthmüller, Efficient iterative schemes for *ab initio* total-energy calculations using a plane-wave basis set, Phys. Rev. B 54 (16) (1996) 11169–11186, http://dx.doi.org/10.1103/physrevb.54.11169.

[49] G. Kresse, D. Joubert, From ultrasoft pseudopotentials to the projector augmented-wave method, Phys. Rev. B 59 (3) (1999) 1758–1775, http://dx.doi.org/10.1103/PhysRevB.59.1758.

[50] J.P. Perdew, K. Burke, M. Ernzerhof, Generalized gradient approximation made simple, Phys. Rev. Lett. 77 (18) (1996) 3865–3868, http://dx.doi.org/10.1103/physrevlett.77.3865.

[51] P.E. Blöchl, Projector augmented-wave method, Phys. Rev. B 50 (24) (1994) 17953–17979, http://dx.doi.org/10.1103/PhysRevB.50.17953.

[52] M. Methfessel, A.T. Paxton, High-precision sampling for Brillouin-zone integration in metals, Phys. Rev. B 40 (6) (1989) 3616–3621, http://dx.doi.org/10.1103/physrevb.40.3616.

[53] H.J. Monkhorst, J.D. Pack, Special points for Brillouin-zone integrations, Phys. Rev. B 13 (12) (1976) 5188–5192, http://dx.doi.org/10.1103/PhysRevB.13.5188.

[54] S.S. Quek, Z.H. Chooi, Z. Wu, Y.W. Zhang, D.J. Srolovitz, The inverse Hall–Petch relation in nanocrystalline metals: A discrete dislocation dynamics analysis, J. Mech. Phys. Solids 88 (2016) 252–266, http://dx.doi.org/10.1016/j.jmps.2015.12.012.

[55] S. Hai, E. Tadmor, Deformation twinning at aluminum crack tips, Acta Mater. 51 (1) (2003) 117–131, http://dx.doi.org/10.1016/s1359-6454(02)00367-1.

[56] X. Wu, C. Li, C. Guo, Z. Du, Thermodynamic re-assessment of the Mg–Y binary system coupling with the precipitation sequence during aging process, CALPHAD 71 (2020) 102010, http://dx.doi.org/10.1016/j.calphad.2020.102010.

[57] R.J. Zamora, A.K. Nair, R.G. Hennig, D.H. Warner, Ab initio prediction of environmental embrittlement at a crack tip in aluminum, Phys. Rev. B 86 (6) (2012) 060101(R), http://dx.doi.org/10.1103/physrevb.86.060101.

[58] P. Andric, W. Curtin, New theory for crack-tip twinning in fcc metals, J. Mech. Phys. Solids 113 (2018) 144–161, http://dx.doi.org/10.1016/j.jmps.2018.01.016.

[59] T.C. Ting, Anisotropic Elasticity: Theory and Applications, Oxford University Press, 1996.

[60] A.P. Thompson, H.M. Aktulga, R. Berger, D.S. Bolintineanu, W.M. Brown, P.S. Crozier, P.J. in't Veld, A. Kohlmeyer, S.G. Moore, T.D. Nguyen, R. Shan, M.J. Stevens, J. Tranchida, C. Trott, S.J. Plimpton, LAMMPS - a flexible simulation tool for particle-based materials modeling at the atomic, meso, and continuum scales, Comput. Phys. Comm. 271 (2022) 108171, http://dx.doi.org/10.1016/j.cpc.2021.108171.

[61] Extended modified embedded-atom method interatomic potential for MgY, 2023, URL https://gitlab.com/CompMatSci/xmeam. (Accessed 22 December 2023).

[62] D.Y. Sun, M.I. Mendelev, C.A. Becker, K. Kudin, T. Haxhimali, M. Asta, J.J. Hoyt, A. Karma, D.J. Srolovitz, Crystal-melt interfacial free energies in hcp metals: A molecular dynamics study of Mg, Phys. Rev. B 73 (2) (2006) http://dx.doi.org/10.1103/PhysRevB.73.024116, 024116–12.

[63] X.-Y. Liu, J.B. Adams, F. Ercolessi, J.A. Moriarty, EAM potential for magnesium from quantum mechanical forces, Modelling Simul. Mater. Sci. Eng. 4 (3) (1996) 293–303, http://dx.doi.org/10.1088/0965-0393/4/3/004.

[64] A. Stukowski, Structure identification methods for atomistic simulations of crystalline materials, Modelling Simul. Mater. Sci. Eng. 20 (4) (2012) 045021, http://dx.doi.org/10.1088/0965-0393/20/4/045021.

[65] A. Luque, M. Ghazisaeidi, W.A. Curtin, A new mechanism for twin growth in Mg alloys, Acta Mater. 81 (2014) 442–456, http://dx.doi.org/10.1016/j.actamat.2014.08.052.

[66] G. Laplanche, A. Kostka, O.M. Horst, G. Eggeler, E.P. George, Microstructure evolution and critical stress for twinning in the CrMnFeCoNi high-entropy alloy, Acta Mater. 118 (2016) 152–163, http://dx.doi.org/10.1016/j.actamat.2016.07.038.

[67] J.F. Nie, Y. Zhu, J. Liu, X.-Y. Fang, Periodic segregation of solute atoms in fully coherent twin boundaries, Science 340 (6135) (2013) 957–960, http://dx.doi.org/10.1126/science.1229369.

[68] S.R. Agnew, M.H. Yoo, C.N. Tomé, Application of texture simulation to understanding mechanical behavior of Mg and solid solution alloys containing Li or Y, Acta Mater. 49 (20) (2001) 4277–4289, http://dx.doi.org/10.1016/S1359-6454(01)00297-X.

[69] Q. Peng, J. Meng, Y. Li, Y. Huang, N. Hort, Effect of yttrium addition on lattice parameter, Young's modulus and vacancy of magnesium, Mater. Sci. Eng. A 528 (4–5) (2011) 2106–2109, http://dx.doi.org/10.1016/j.msea.2010.11.042.

[70] C.H. Cáceres, D.M. Rovera, Solid solution strengthening in concentrated Mg–Al alloys, J. Light Metals 1 (3) (2001) 151–156, http://dx.doi.org/10.1016/S1471-5317(01)00008-6.

[71] C.H. Cáceres, A. Blake, The strength of concentrated Mg–Zn solid solutions, Phys. Status Solidi (a) 194 (1) (2002) 147–158, http://dx.doi.org/10.1002/1521-396X(200211)194:1<147::AID-PSSA147>3.0.CO;2-L.

[72] N. Stanford, M.R. Barnett, Solute strengthening of prismatic slip, basal slip and $\{10\bar{1}2\}$ twinning in Mg and Mg–Zn binary alloys, Int. J. Plast. 47 (Supplement C) (2013) 165–181, http://dx.doi.org/10.1016/j.ijplas.2013.01.012.

[73] S. Sandlöbes, M. Friák, S. Korte-Kerzel, Z. Pei, J. Neugebauer, D. Raabe, A rare-earth free magnesium alloy with improved intrinsic ductility, Sci. Rep. 7 (1) (2017) 10458, http://dx.doi.org/10.1038/s41598-017-10384-0.

[74] Y. Chai, B. Jiang, J. Song, Q. Wang, J. He, J. Zhao, G. Huang, Z. Jiang, F. Pan, Role of Al content on the microstructure, texture and mechanical properties of Mg–3.5Ca based alloys, Mater. Sci. Eng. A 730 (2018) 303–316, http://dx.doi.org/10.1016/j.msea.2018.06.011.

[75] J.D. Robson, N. Stanford, M.R. Barnett, Effect of precipitate shape on slip and twinning in magnesium alloys, Acta Mater. 59 (5) (2011) 1945–1956, http://dx.doi.org/10.1016/j.actamat.2010.11.060.

[76] J.J. Bhattacharyya, F. Wang, P.D. Wu, W.R. Whittington, H. El Kadiri, S.R. Agnew, Demonstration of alloying, thermal activation, and latent hardening effects on quasi-static and dynamic polycrystal plasticity of Mg alloy, WE43-T5, plate, Int. J. Plast. 81 (2016) 123–151, http://dx.doi.org/10.1016/j.ijplas.2016.01.005.

[77] Z. Zhang, J. Zhang, W. Wang, S. Liu, B. Sun, J. Xie, T. Xiao, Unveiling the deformation mechanism of highly deformable magnesium alloy with heterogeneous grains, Scr. Mater. 221 (2022) 114963, http://dx.doi.org/10.1016/j.scriptamat.2022.114963.

[78] X. Wang, J. Wang, Y. He, C. Wang, L. Zhong, S.X. Mao, Unstable twin in body-centered cubic tungsten nanocrystals, Nature Commun. 11 (1) (2020) http://dx.doi.org/10.1038/s41467-020-16349-8, 2497–2497.